Ding *et al.*
Chinese Journal of Mechanical Engineering (2024) 37:98
https://doi.org/10.1186/s10033-024-01080-y

Chinese Journal of Mechanical Engineering

ORIGINAL ARTICLE

Open Access

Enhancing the Robustness of Rib-Groove Filling and Strain Homogeneity in the Isothermal Forging of Titanium Alloy Multi-Rib Components

Tong Ding[1], Ke Wei[1,2*], Yong Hou[2], Xianjuan Dong[1], Long Huang[1] and Myoung-Gyu Lee[2*]

Abstract

Isothermal forging stands as an effective technology for the production of large-scale titanium alloy multi-rib components. However, challenges have persisted, including die underfilling and strain concentration due to the complex material flow and heterogeneous deformation within the forging die cavity. While approaches centered on optimized billet designs have mitigated these challenges, uncertainties in process parameters continue to introduce unacceptable variations in forming accuracy and stability. To tackle this issue, this study introduced a multi-objective robust optimization approach for billet design, accounting for the multi-rib eigenstructure and potential uncertainties. The approach includes finite element (FE) modeling for analyzing the die-filling and strain inhomogeneity within the multi-rib eigenstructure. Furthermore, it integrated image acquisition perception and feed back technologies (IAPF) for real-time monitoring of material flow and filling sequences within die rib-grooves, validating the accuracy of the FE modeling. By incorporating dimensional parameters of the billet and uncertainty factors, including friction, draft angle, forming temperature, speed, and deviations in billet and die, quantitative analyses on the rib-groove filling and strain inhomogeneity with fluctuation were conducted. Subsequently, a dual-response surface model was developed for statistical analysis of the cavity filling and strain homogeneity. Finally, the robust optimization was processed using a non-dominated sorting genetic algorithm II (NSGA-II) and validated using the IAPF technologies. The proposed approach enables robust design enhancements for rib-groove filling and strain homogeneity in titanium alloy multi-rib components.

Keywords Titanium alloy multi-rib components, Die rib-groove filling, Strain homogeneity, Multi-objective robust optimization, Real-time monitoring

1 Introduction

Large-scale Ti-alloy rib-web components (LTRC) are highly desirable in aerospace and transportation due to their advantageous properties such as high specific strength, high specific stiffness, good corrosion resistance, and lightweight characteristics [1]. However, the complexity of these components, which consist of multiple ribs and thin webs, introduces challenges in the forging process. Factors such as the multi-rib asymmetric structure, interactions among process parameters, and coupling of multiple physical fields need to be carefully

*Correspondence:
Ke Wei
weike@nchu.edu.cn
Myoung-Gyu Lee
myounglee@snu.ac.kr
[1] School of Aeronautical Manufacturing Engineering, Nanchang Hangkong University, Nanchang 330063, China
[2] Department of Materials Science and Engineering & RIAM, Seoul National University, Seoul 08826, Republic of Korea

considered. Failure to address these factors can result in intricate material flow and significant strain inhomogeneity within the forging die cavity. To ensure precise integration of macro and micro formability and achieve high forming quality and integrity of LTRC, special attention must be given to the material flow, die rib-groove filling, and strain homogeneity throughout the entire component [2, 3].

To date, studies on plastic forming have been conducted based on the concepts of flexible and digital manufacturing. Kampen et al. [4] proposed a performance optimization method for cross-wedge rolling using a genetic algorithm to overcome the reliance on the experience of engineers and the time-consuming optimization process. Nayak et al. [5] minimized strain and temperature heterogeneity and addressed fishtail defects during the ring rolling process using a response surface approach. Han et al. [6] introduced an innovative approach for optimizing the design of precast billets in the context of forging processes, incorporating non-uniform rational basis spline (NURBS), finite element (FE) analysis, and genetic algorithm techniques to achieve desirable material flow and strain homogeneity during forging. Zheng et al. [7] proposed a design-based approach to analyze, predict, and mitigate folding defects in forming processes, focusing on investigating the relationship between folding defect formation mechanisms and dimensional effects to effectively control flow and strain distribution. Wei et al. [8] optimized the initial volume distribution of unequal-thickness billet (UTB) using the Box-Behnken design and response surface model to mitigate the occurrence of folding defects in the transitional region of isothermal local loading for LTRC. In this study, Figure 1 illustrates the introduction of LTRC and the development of manufacturing technology. Advanced

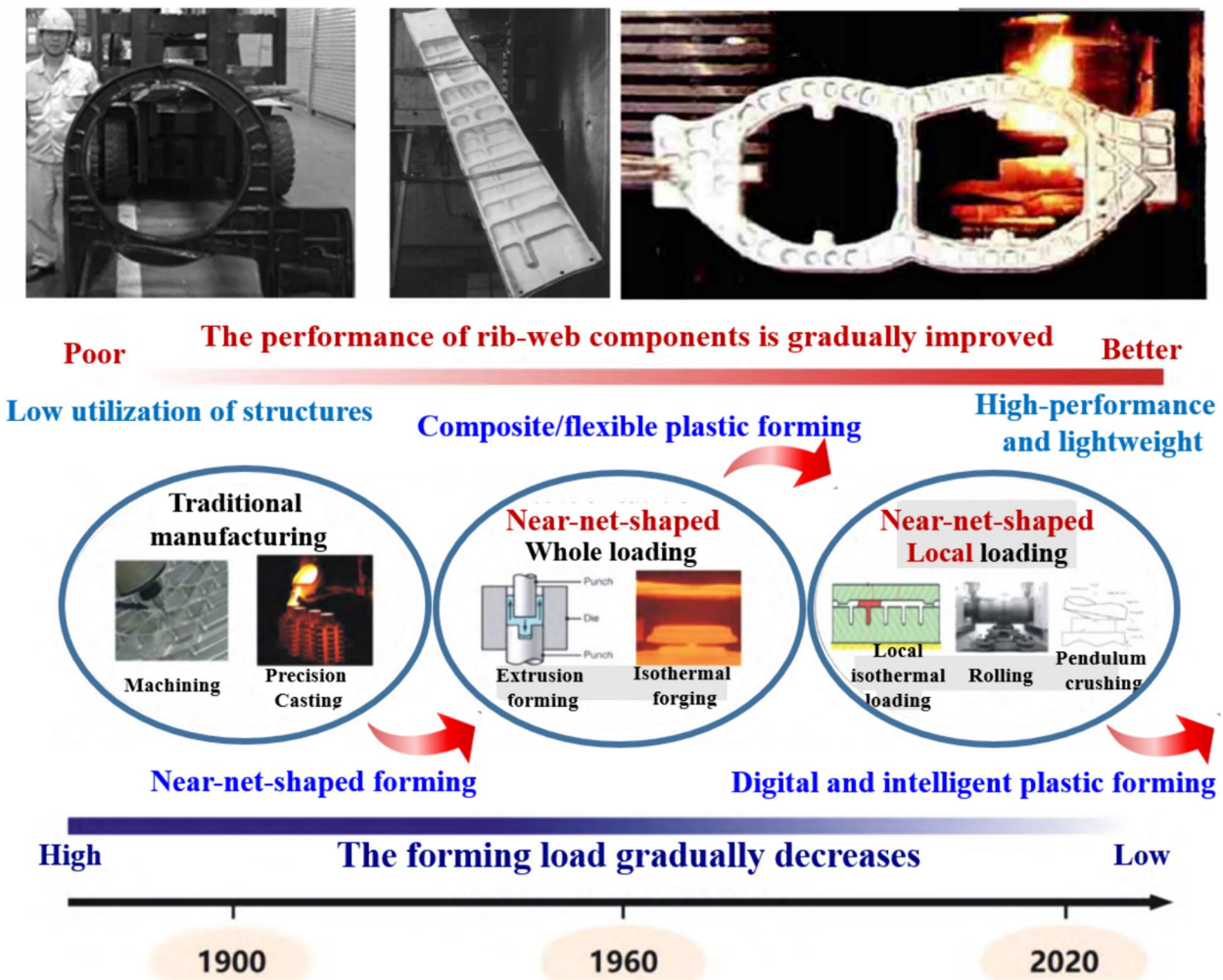

Figure 1 Introduction of LTRC and the development history of manufacturing technology

digital and intelligent manufacturing technologies have been developed for achieving high precision, high efficiency, and high-quality components throughout the entire process of plastic forming [9, 10].

While these flexible forming studies primarily focus on billet influence design, which is undoubtedly a meaningful task, comprehensive consideration must also be given to the robustness of filling characteristics and strain homogeneity for multi-rib components under the influence of uncertainties related to process parameters. These uncertainties include variations in billet and die manufacturing, equipment conditions, and lubrication. Similarly, Hou et al. [11] constructed a dual-response surface model for the mean and variance of fracture and wrinkling resistance with drawing rib and the crimping force. They incorporated uncertainty factors such as the material hardening index, anisotropy index, and friction coefficient to achieve robust optimization for the inner lid of luggage compartments. Li et al. [12] proposed a robust design method for computer numerical control bending and forming parameters of large-diameter thin-walled aluminum tubes, considering the effects of noise factors such as material parameters, friction parameters, and tube geometry parameter fluctuations. In comparison with the focus on die rib-groove filling and strain homogeneity, these aforementioned studies differ in terms of their process parameters and forming results.

Furthermore, due to the rapid advancement of artificial intelligence technology, the field of smart manufacturing has undergone significant development. Smart manufacturing is characterized by autonomous monitoring and sensing, autonomous learning and modeling, autonomous optimization and decision-making, autonomous control, and execution of complex forming processes. In the manufacturing process, the integration of physical information systems enables equipment to carry out intelligent decision-making and adaptive control of processing conditions, effectively ensuring forming quality. Park et al. [13] introduced data clustering-based machine learning (ML) to predict process thickness in steel plate ring-rolling operations, combining clustering algorithms and supervised learning algorithms to propose ML techniques. Bader et al. [14] investigated various methods of measuring bending curvature by comparing optical, tactile, and electromagnetic induction tests, correlating bending measurements with open-loop control to propose an optimal method for measuring bent steel strips for an automatic straightening process.

Online monitoring and perception of component quality based on intelligent forming processes, including autonomous monitoring and sensing, autonomous learning and modeling, autonomous optimization and decision making, autonomous control and execution of complex forming processes (Figure 2) [15]. Cuartas et al. [16] aimed to develop an ML algorithm to classify steel casting for tire reinforcement based on the number and properties of inclusions. Zhang et al. [17] investigated the in-situ evaluation of surface residual compressive stress for 7075 aluminum alloy in laser shock peening and efficient sensing of acoustic emission using a deep ML method. Cho et al. [18] presented a real-time anomaly detection method that uses a convolutional neural network (CNN) that creates CNN-based models that detect abnormalities by learning from melt pool image data pre-processed to enhance learning performance. According to Baral et al. [19], custom-made acoustic admission sensors employing piezoelectric crystals were implemented to measure the emitted acoustic signal during uniaxial tension and cup drawing tests of an AA6013-T4 aluminum sheet, showing accurate identification of necking onset and fracture location prediction. Gao et al. [20] proposed a novel online intelligent design method for roll paths in conventional spinning, achieving multifunctional spinning condition monitoring, real-time prediction of spinning status, online dynamic processing optimization, and the instantaneous execution of optimal processing. This method is highly efficient and economically promotes the application of spinning technology.

Current research indicates that the forming and manufacturing of complex components have evolved from traditional trial-and-error methods to flexible, digital, and intelligent technology. It requires increasingly higher efficiency and highly demanding forming quality to achieve high-performance and lightweight structures. However, the accuracy and stability of forming achieved through intelligent technology for plastic deformation may be unacceptable if practical uncertainty factors are not considered Therefore, it is essential to develop a robust optimization method for billet design that is scientifically and quantitatively based, considering the fluctuation of uncertainty factors.

To achieve these goals, uncertainty analysis and multi-objective robust optimization must be integrated into the optimization process. However, experiment-based examination of uncertainty factors is challenging because they cannot be defined during the actual forging process, not to mention the high experimental cost and low efficiency. In this study, FE simulations based on the Deform-3D platform were conducted using TA15 eigenstructure as the study object to reveal the material flow law, filling sequence of die rib-grooves, and strain homogeneity during the isothermal forging process. Meanwhile, image acquisition perception and feedback (IAPF) technologies for online monitoring were incorporated to capture the material filling in the rib-grooves and provide real-time feedback on the filling sequence of each rib-groove

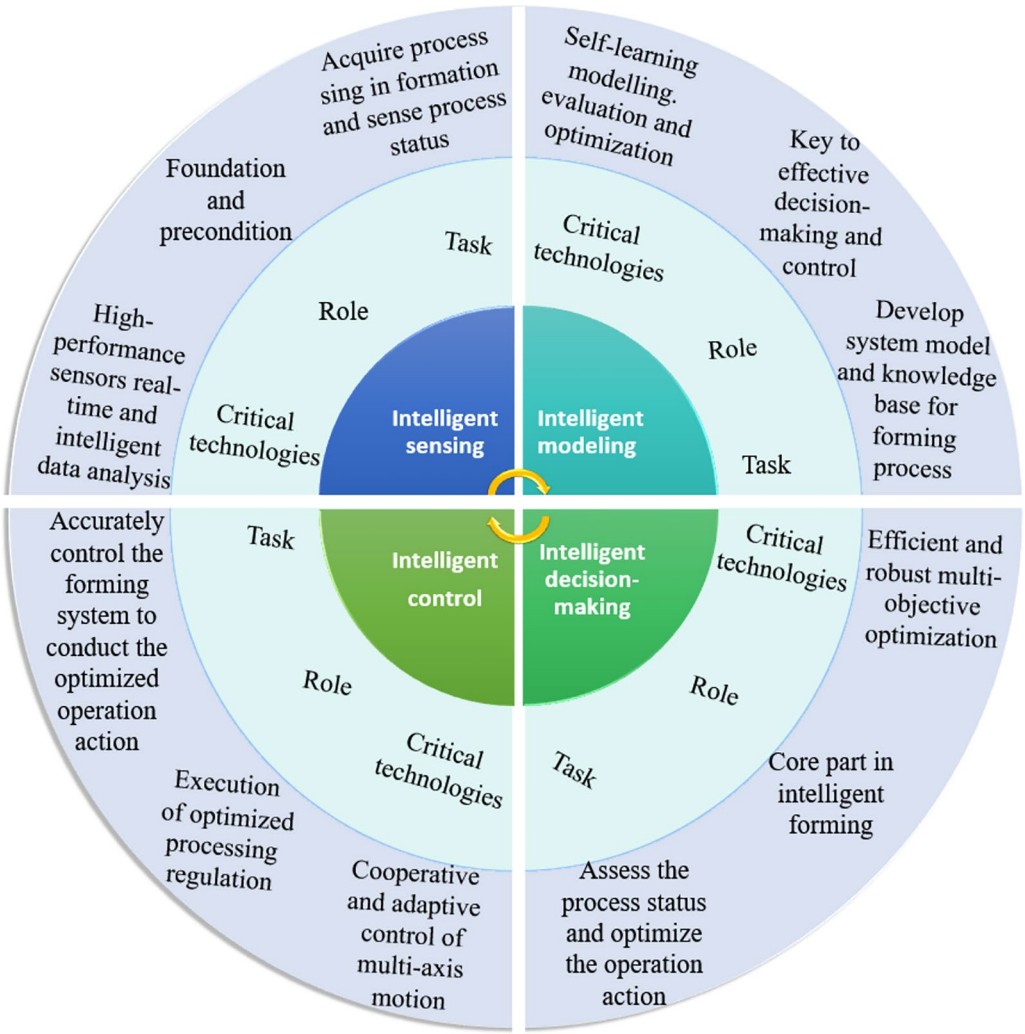

Figure 2 Schematic of key functions of intelligent forming

in its actual state. Subsequently, multi-objective billet robust optimization was developed to improve the mean and standard deviation (SD) of rib-groove filling and strain homogeneity based on the dual-response surface methodology (RSM). Finally, based on the plasticine experiments, the robust optimization solution of each parameter was conducted and then verified using both IAPF technologies and FE analysis.

2 FE Modle Details and Intelligent Perception Formation

2.1 FE Modeling and Real-Time Monitoring

2.1.1 FE Modeling

The structural characteristics of LTRC are characterized by their large size, integration, thin-walled construction, and multiple ribs, where the rib width, rib height, and rib spacing exhibited significant variations in an extremely complex shape, as depicted in Figure 3a, b [21–24]. The study focused on a multi-rib component, as shown in Figure 3c, which represents the typical characteristics of such components.

Furthermore, during the forming process, materials experienced cross-flow in the web and a reverse flow of material in the rib-grooves [25, 26]. The non-flash die forging and constant volume principle of the billet were adopted. The simple equal-thickness billet (ETB) as well as UTB were selected to observe the material flow in the die rib-grooves. As shown in Figure 3, the eigenstructure was extracted based on the structural characteristics of LTRC. In the FE modeling, half of the die was adopted due to the symmetrical surface

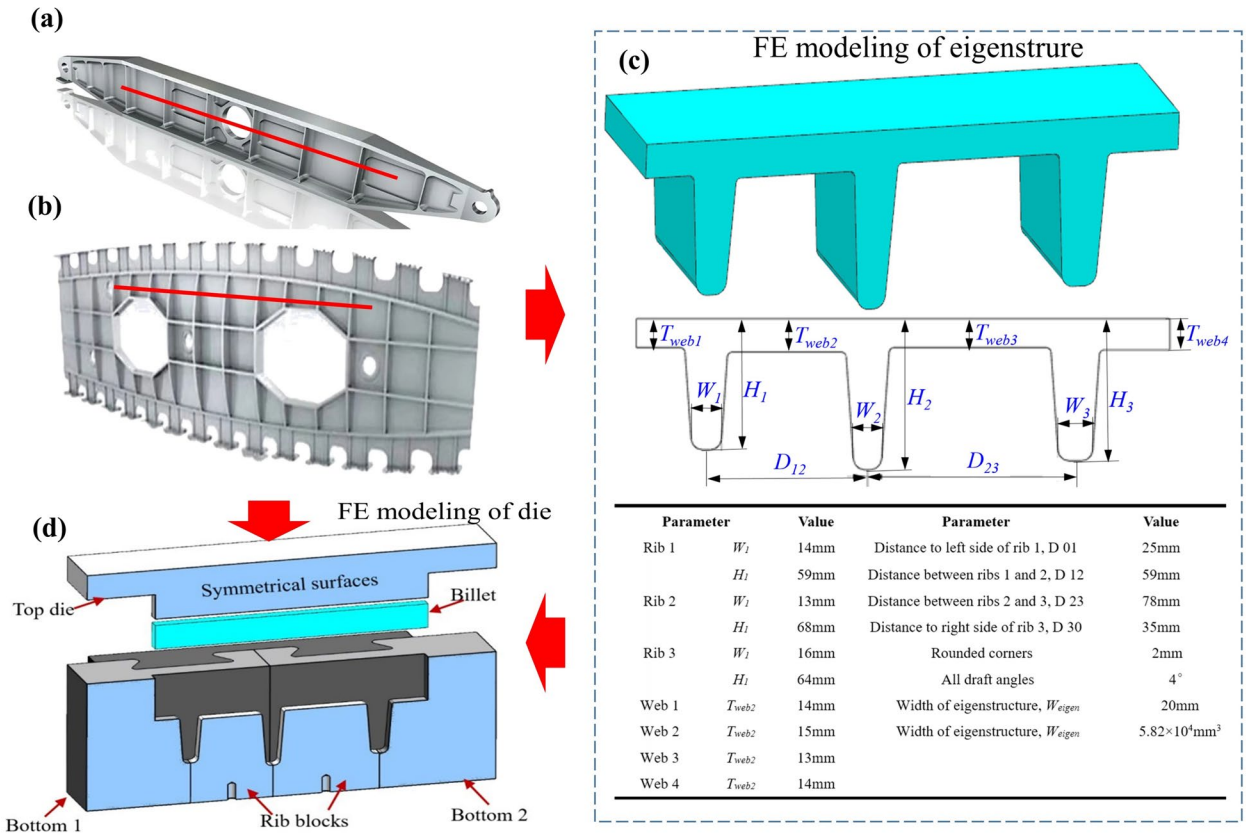

Parameter		Value	Parameter	Value
Rib 1	W_1	14mm	Distance to left side of rib 1, D 01	25mm
	H_1	59mm	Distance between ribs 1 and 2, D 12	59mm
Rib 2	W_1	13mm	Distance between ribs 2 and 3, D 23	78mm
	H_1	68mm	Distance to right side of rib 3, D 30	35mm
Rib 3	W_1	16mm	Rounded corners	2mm
	H_1	64mm	All draft angles	4°
Web 1	T_{web2}	14mm	Width of eigenstructure, W_{eigen}	20mm
Web 2	T_{web2}	15mm	Width of eigenstructure, W_{eigen}	5.82×10^4mm^3
Web 3	T_{web2}	13mm		
Web 4	T_{web2}	14mm		

Figure 3 Description of the FE model: **a**, **b** LTRC components, **c** Eigenstructure, **d** Die geometry

Table 1 Simulation setting

	Parameter	Values
Billet	Material	TA15
	Forming temperature	950–980 ℃
	Number of elements	60000
Die	Material	Rigid
	Temperature	Associated with billets
	Speed	0.2 mm/s
Boundary conditions	Friction factor	0.39–0.41
	Heat transfer coefficient	–
	Stroke increment	0.2 mm/step
	Symmetry plan	(0–10.0)

in the middle of the eigenstructure (Figure 3d). The rigid-plastic method was utilized because the deformation of the workpiece was much larger than that of the die. The billet serves as a plastic body and the die serves as a rigid body. Due to the low strain rate in isothermal forging, deformation, and frictional heat generation, temperature transfer was neglected. To approximate the complex geometry of the component accurately, and facilitate better material flow in the die rib-grooves, the billet was discretized using tetrahedral elements. Specific simulation parameter settings are shown in Table 1.

2.1.2 Implementation of Online Monitoring

In actual working conditions, equipping the forming equipment with an intelligent decision-making and adaptive control system is advantageous for obtaining defect-free components with high forming quality. The online perception of the shape and properties of components in the external fields of plasticity processing (e.g. thermal, force, and special energy such as magnetism and light), involves integrating numerical simulation of the forming process with intelligent technology. Through online measurement of physical quantities, such as force, heat, in-depth sensing, and prediction of product shape and property changes, feedback and active control were used to digitally display or predict the forming process of complex components, thus achieving real-time monitoring functions. In this study, physical simulation experiments (PSE) of the forming process were monitored to provide real-time feedback on the die-filling status (Figure 4). To

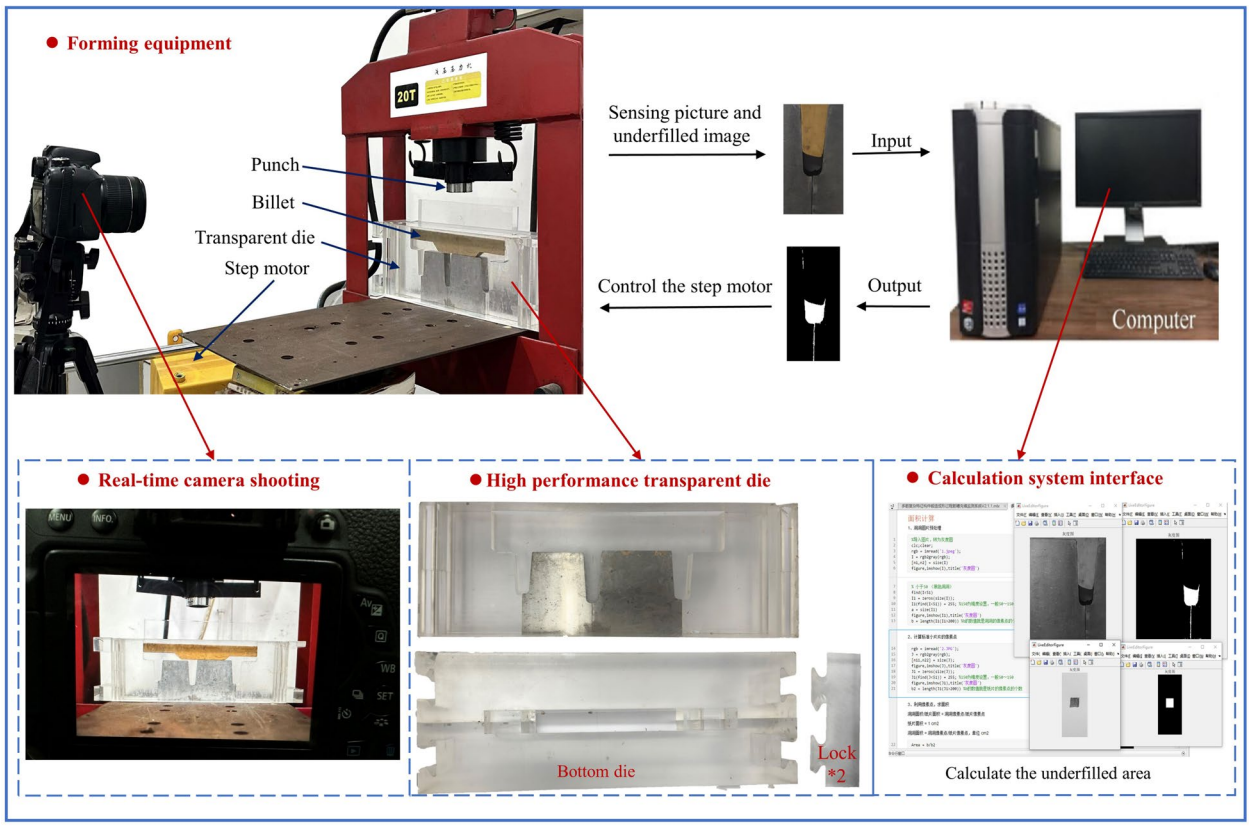

Figure 4 Implementation of real-time online monitoring

ensure clear image recognition and online monitoring of material flow in the die rib-grooves, a high-performance transparent die set was manufactured. The online monitoring using image analysis of plastic flow (IAPF) technologies involves four steps, as summarized below:

(1) The billet was deformed through the transparent die by controlling the step motor.
(2) A high-pixel camera was used for photography or videography. Thus, the photograph was captured during the die-filling process.
(3) Based on the IAPF techniques, the photograph was thus transmitted in real-time and analyzed using MATLAB software. Meanwhile, a reference mark unit was set on the die.
(4) The underfilling volume is determined based on the actual underfilling area and the die cavity thickness, as described in Eq. (1). Eq. (2) is employed to calculate the die underfilling rate for online monitoring. Moreover, Figure 5 shows that the underfilling volume in the ribs was equated to the depressed vol-

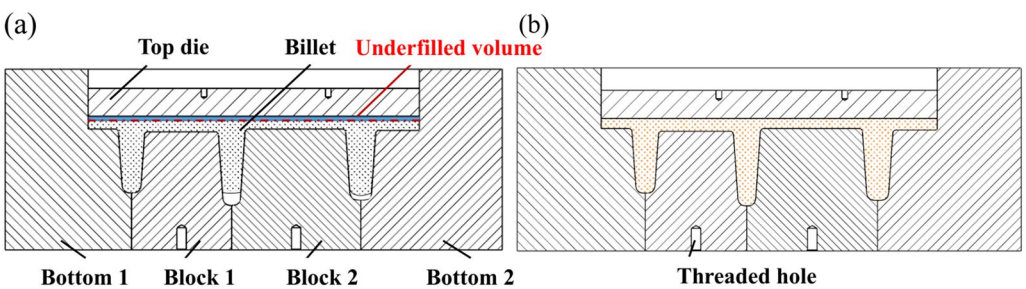

Figure 5 The drawing of eigenstructure: **a** A rib groove is filled (**b**) All ribs are fully-filled [26]

ume of the web in the process between the first rib and the all rib being filled [26].

$$V_{underfill} = \left(Ni/N_{unit}\right) \times S_{unit} \times h, \tag{1}$$

$$\Phi_f = \left(V_{underfill}/V_{eigen}\right) \times 100\%, \tag{2}$$

where N_i is the number of pixel points in the rib-grooves. N_{unit} is the number of pixel points per unit area reference mark. S_{unit} is the area of pixel points per unit area reference mark. h is the cavity thickness. $V_{underfill}$ is the underfilling volume and V_{eigen} is the ideal volume of eigenstructure. It was evident that the closer Φ_u to 0, the better the filling of the die rib-grooves.

Notably, the captured information image was pixel-dotted based on a grey conversion algorithm, followed by the setting of a determination threshold to filter and classify the scattered pixel dots. The actual underfilling area was calculated by comparing the number of filtered unfilled pixel points with the number of pixel points per unit area of the reference marker.

2.1.3 Experimental Validation Based on IAPF Techniques

In previous physical simulations, researchers often used soft materials such as pure plasticine or lead instead of Ti-alloy to conduct actual operations. They analyzed the material flow and observed the defects generated during the forming process, providing practical validation for FE simulation analysis [27, 28]. Sofuoglu et al. [29] showed that pure plasticine with low flow stresses was used in some simple experiments for 2D and 3D physical modeling analysis. Sun et al. [30] utilized pure plasticine to verify the strain inhomogeneity patterns of composite cavity forming under complex loading paths, proposing a composite cavity forming path to prevent folding defects. Cao et al. [31] analyzed the feasibility of forming complex multi-cavity components of 316LN steel through plasticine PSE, considering both geometric and process parameters. Therefore, plasticine was also employed in this study to predict material flow and observe die rib-groove filling, enhancing experiment efficiency and reducing experiment costs.

In this study, plasticine PSE was utilized. The material flow in the die rib-grooving cavity was observed after exerting pressure on plasticine. The constitutive models that describe the deformation behavior of plasticine mainly include:

(a) Considering the effects of strain and strain rate on the plasticine deformation, plasticine is assumed to be elastic-plastic, with flow characteristics described by an exponential equation [32]:

$$\sigma = K\varepsilon^n\dot{\varepsilon}^m, \tag{3}$$

where σ is the flow stress, n is the strain hardening exponent, m is the strain rate sensitivity exponent, and K is the strength coefficient.

(b) Considering the temperature, strain, and strain rate simultaneously, plasticine is assumed to be a visco-plastic body, whichdescribed by the Norton–Hoff equation [33]:

$$\sigma = K\varepsilon^n\dot{\varepsilon}^m e^{-\beta T}, \tag{4}$$

where σ is the flow stress, n is the strain hardening exponent, m is the strain rate sensitivity exponent, and K and β are material constants.

According to Sofuoglu et al. [34], the plastic deformation behavior of plasticine at room temperature can be approximated using Eq. (5).

Table 2 Performance parameters of plasticine and TA15

Materials	Performance specification	Experimental temperature	Strain-hardening	Strain rate	References
Plasticine	$\sigma = K\varepsilon^n$	25 ℃	0 – 0.167	–	[32]
			0.224		[34]
			0.183		[35]
			0.4738,0.3789		[35]
	$\sigma = K\varepsilon^n\dot{\varepsilon}^m$	25 ℃	0.07	0.17	[36]
			0.19 – 0.24	0.16–0.24	[37]
	$\sigma = K\varepsilon^n\dot{\varepsilon}^m e^{-\beta T}$	24–40 ℃	0.085	0.175	[33]
TA15	$\sigma = \sigma(\bar{\varepsilon}, \dot{\bar{\varepsilon}}, T)$	900–1000 ℃	0.1–0.5	0.1–0.5	

Table 3 The material parameters of plasticine in FE simulations

No.	1	2	3	4	5	6
K (MPa)	0.1	0.2	0.14	0.145	0.15	0.15
n	0.3	0.3	0.25	0.25	0.25	0.3

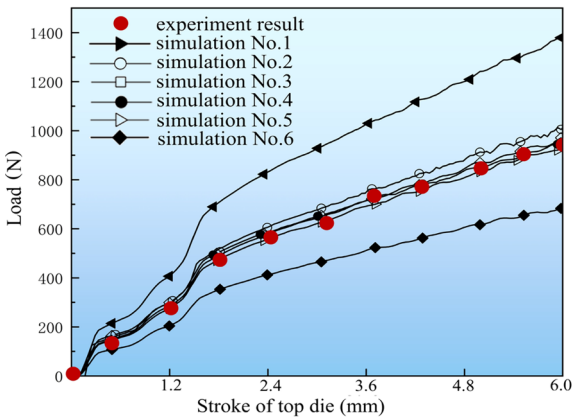

Figure 6 Relationship between the load and stroke

$$\sigma = K\varepsilon^n, \tag{5}$$

where K is the material strength coefficient, and n is the strain-hardening exponent (about 0.1–0.3). Table 2 presents the performance parameters of plasticine and TA15, which were used for the next validation of FE modeling.

Furthermore, based on previous research on plasticine, the trial-and-error principle was used to obtain the model parameters. Table 3 presents the material properties of plasticine in FE simulation. Meanwhile, the relationship between the deformation and load of plasticine was obtained by combining PSE and FE simulation. Figure 6 illustrates the calculated curves for numbers two, three, four, and five, which were consistent with the experiment result. Meanwhile, the experimental scatter points merely fluctuated between numbers four and five. Therefore, K was chosen as 0.145 or 0.15, while n was chosen as 0.25.

Given the above constitutive models, the corresponding FE-Plasticine and FE-TA15 were established for the PSE. Consequently, the reliability of these FE models was verified. Figure 7 shows the forming and real-time feedback results at different forming stages. It was observed that the rib-grooves filling sequence of plasticine in the PSE process was Rib 3 > Rib 1 > Rib 2. Compared with plasticine and TA15 in FE simulation, the material flow and die-filling sequence were consistent with each other. Moreover, the material flow of plasticine in FE simulation closely aligns with that of the physical simulation verification.

The simulation results of FE-Plasticine and FE-TA15 indicated that the deformation characteristics of components with multi-rib were similar during the forming process for different materials. The PSE of plasticine indicated that FE simulation of macroscopic material flow law of TA15 multi-rib eigenstructure during the high-temperature forming process is valid and can be used effectively for the next robust optimization.

Figure 8 provides a comparison of underfilling rates among the PSE and FE simulations. It was observed that the underfilling rates of three ribs using FE-Plasticine and FE-TA15 were basically in agreement. Meanwhile, the underfilling rate trend of each rib-groove for the plasticine in PSE was consistent with that of FE-Plasticine. This further demonstrated that plasticine was used instead of TA15 alloy to observe material flow in the multi-rib eigenstructure.

2.2 Detailed Procedure of Multi-objective Robust Optimization

Many uncertainties in the actual forming process can lead to deviations in forming quality, such as billet manufacturing deviations, temperature variations, material and equipment losses, and manual errors. Therefore, it was necessary to consider the +influence of uncertainties on the forming results in the isothermal forging of LTRC [38–40]. Combining BBD, FE simulation method, dual-RSM, and NSGA-II, the multi-objective billet robust optimization under image perception and online monitoring was based on IAPF, was proposed. This approach aims to achieve robust control of filling and strain homogeneity (Figure 9).

3 Online Intelligent Modelling Based on Dual-RSM

3.1 Determination of Significant Factors and Responses

3.1.1 Selection of Significant Factors Based on Orthogonal Experiment

In the process of analyzing the experimental results, the range analysis method was employed to evaluate the influence and significance of the uncertainty factors on the target value. As an illustrative example, the uncertainty factor A was used.

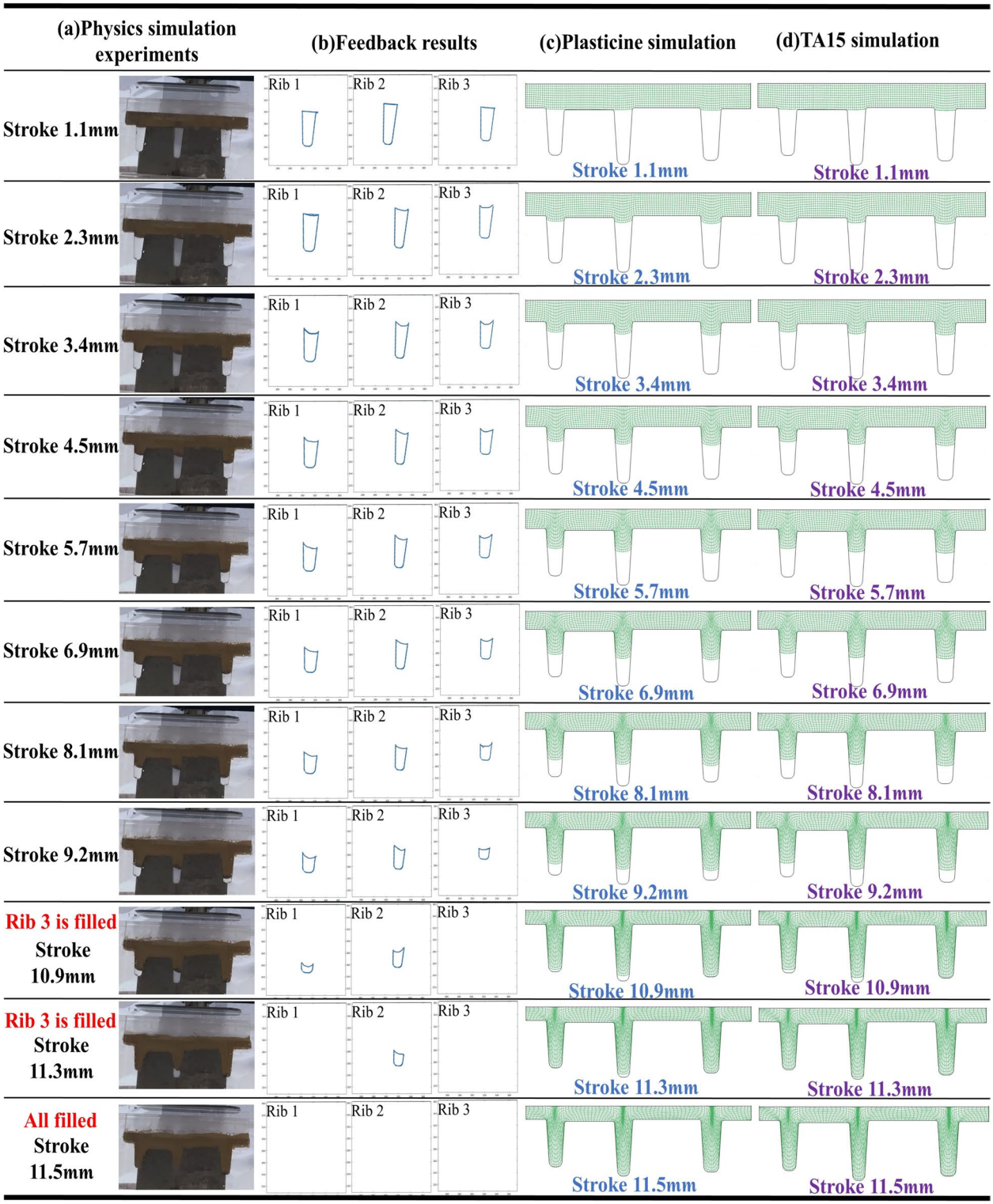

Figure 7 Results of physical simulation experiment and FE simulation by different material models: **a** Physical experiments, **b** Feedback results, **c** FE-Plasticine, **d** FE-A15

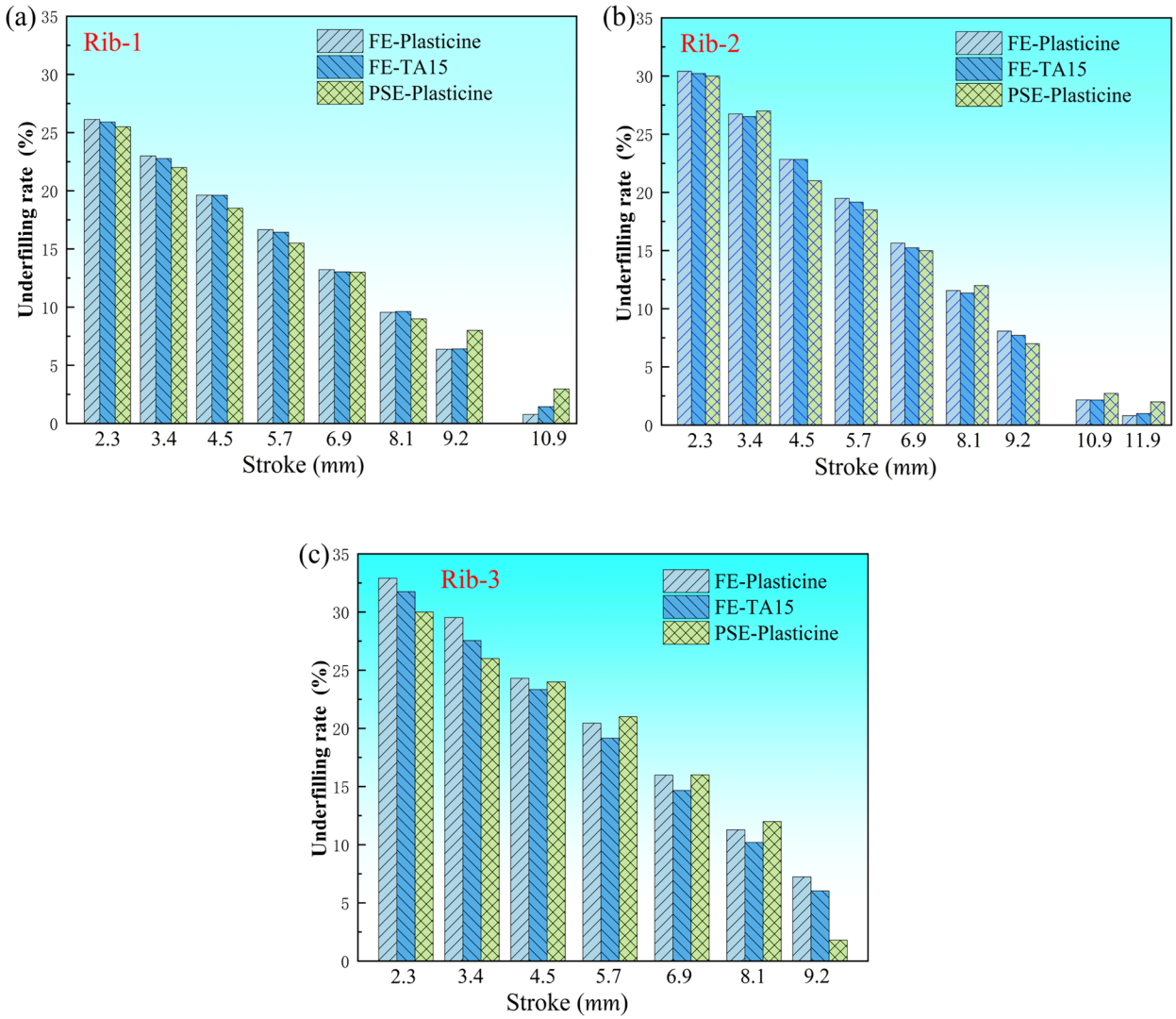

Figure 8 The comparison of underfilling rate among the PSE and FE simulations: **a** Rib-1, **b** Rib-2, **c** Rib-3

$$\begin{cases} K_{A1} = Y(1) + Y(2) + Y(3), \overline{K}_{A1} = K_{A1}/3, \\ K_{A2} = Y(4) + Y(5) + Y(6), \overline{K}_{A2} = K_{A2}/3, \\ K_{A3} = Y(7) + Y(8) + Y(9), \overline{K}_{A3} = K_{A3}/3, \end{cases} \tag{6}$$

$$R_j = \max\left(\overline{K}_{Ai}\right) - \min(\overline{K}_{Ai}), \tag{7}$$

where K_{Ai} is the i_{th} level of factor A ($I = 1, 2, 3$); $Y(P)$ is the P_{th} test in Table 4 (P = 1, 2, ..., 9). It was observed that K_{ji} is the sum of each factor j ($j = A, B, C, D$), and K_{ji} is the average of each factor at the same level. A higher R_j indicated a more significant factor.

According to Ref. [26], the following six uncertainty factors are selected.

(1) **Die draft angle**: As shown in Figure 10, shear friction is generated on the surface of the die and the billet. It is related to the normal stress of the contact surface. When rib-groove draft angle fluctuates, it will lead to the friction factor fluctuation and eventually affect the material flow.

(2) **Billet manufacturing deviation**: As there exists manufacturing tolerance on the surface of billet, allowing a certain range of variation to occur for the geometric dimensions of billets. Then, the actual billet dimensions may deviate from the ideal values.

(3) **Forming speed**: In the actual process, it is undeniable that a certain range of fluctuation is generated

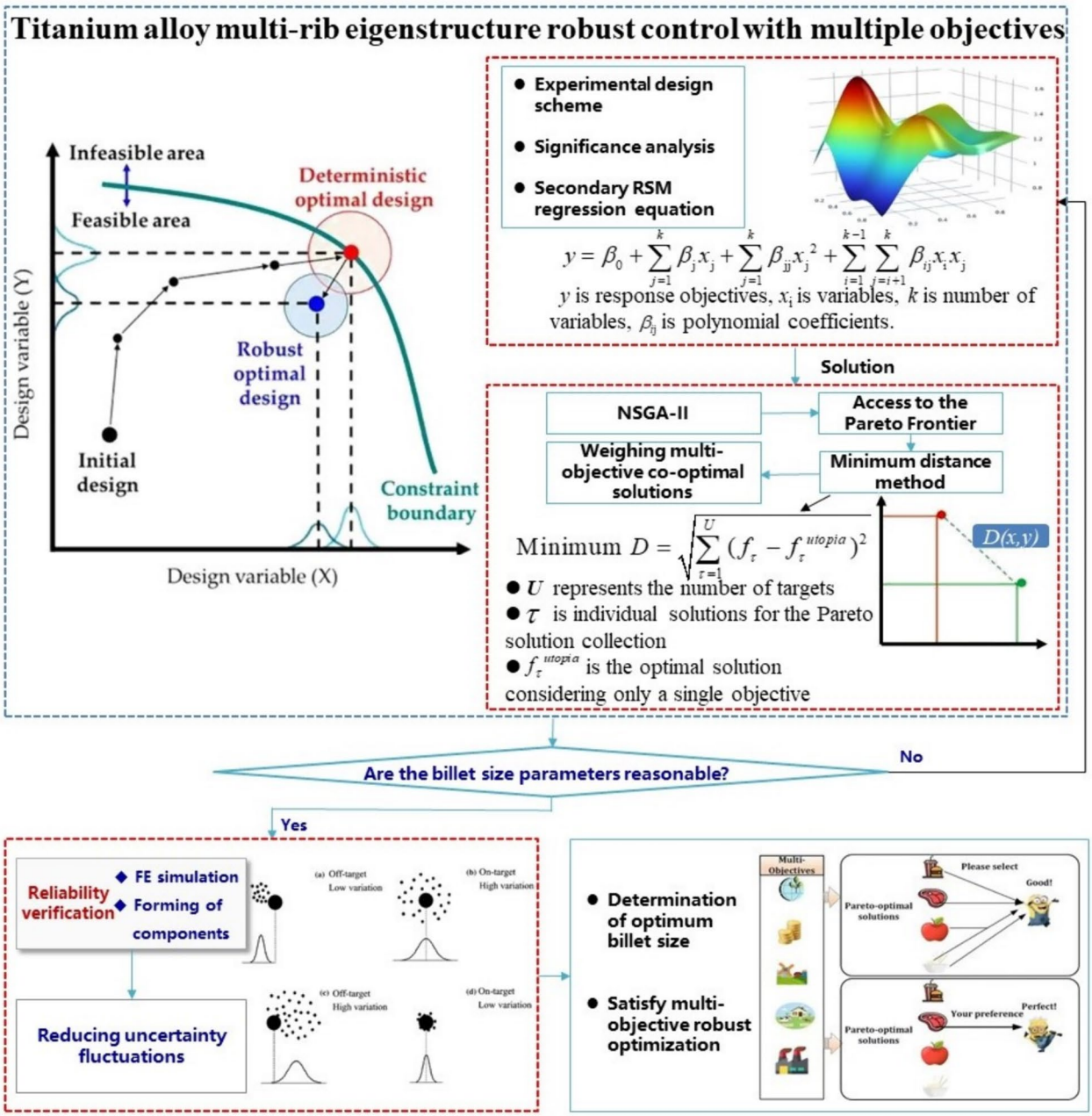

Figure 9 The procedure of multi-objective robust optimization for Ti-alloy multi-rib eigenstructure

in the stroke speed of upper die under the comprehensive influence of factors such as friction fluctuation, equipment wear, and human operation.

(4) **Die manufacturing deviation**: As shown in Figure 10, a certain assembly clearance as well as manufacturing tolerances may be considered after the die is manufactured, because the die manufacturing deviation will also affect the forming accuracy.

(5) **Forming temperature**: The heat transfer can be produced among the dies, the billet, the environment as well as the shear friction between the billet and the die, which are generated during the forming

Table 4 Orthogonal experiment design array $L25(5^6)$

Test	Uncertainty factors						Underfilling Rate Φ_f (%)	Strain homogeneity Φ_s
	Rib-groove draft angle (°)	Billet Manufacturing deviation (mm)	Forming Speed (mm/s)	Die Manufacturing deviation (mm)	Forming Temperature (℃)	Friction factor		
1	3.90	− 0.1	0.10	− 0.1	950.0	0.390	3.36	1.562
2	3.90	− 0.05	0.15	− 0.05	957.5	0.390	2.94	1.677
3	3.90	0	0.20	0	965.0	0.390	2.91	1.121
4	3.90	0.05	0.25	0.05	972.5	0.390	2.81	1.134
5	3.90	0.1	0.30	0.1	980.0	0.390	2.65	1.137
6	3.95	− 0.1	0.15	0	972.5	0.395	2.76	1.182
7	3.95	− 0.05	0.20	0.05	980.0	0.395	3.62	1.088
8	3.95	0	0.25	0.05	950.0	0.395	3.45	1.096
9	3.95	0.05	0.30	− 0.1	957.5	0.395	2.39	1.569
10	3.95	0.1	0.10	− 0.05	965.0	0.395	2.56	1.925
11	4.00	− 0.1	0.20	0.1	957.5	0.400	3.15	1.145
12	4.00	− 0.05	0.25	− 0.1	965.0	0.400	2.37	1.605
13	4.00	0	0.30	− 0.05	965.0	0.400	3.06	1.087
14	4.00	0.05	0.10	0	972.5	0.400	2.86	1.103
15	4.00	0.1	0.15	0.05	950.0	0.400	2.57	1.116
16	4.05	− 0.1	0.20	− 0.05	980.0	0.405	3.13	1.137
17	4.05	− 0.05	0.30	0	950.0	0.405	2.95	1.140
18	4.05	0	0.10	0.05	957.5	0.405	2.75	1.172
19	4.05	0.05	0.15	0.1	965.0	0.405	3.32	1.085
20	4.05	0.1	0.20	− 0.1	972.5	0.405	2.48	1.108
21	4.10	− 0.1	0.30	0.05	965.0	0.410	3.42	1.097
22	4.10	− 0.05	0.10	0.1	972.5	0.410	3.26	1.116
23	4.10	0	0.15	− 0.1	972.5	0.410	2.32	1.140
24	4.10	0.05	0.20	− 0.05	950.0	0.410	2.25	1.198
25	4.10	0.1	0.25	0	957.5	0.410	2.94	1.081

process, allowing certain fluctuations of the forming temperature to be developed under the combined effect of frictional heat generation and heat transfer.

(6) **Friction factor**: According to Ref. [49], the friction factor can affect the material flow in the die forging; therefore, the fluctuation of the friction factor is considered in this work.

The effects of the uncertainty factors on the underfilling rate and strain homogeneity are presented in Figure 10. The results indicated that the billet manufacturing deviation, the die manufacturing deviation, and the friction factor exhibited significant impacts on both underfilling rate and strain homogeneity. However, the draft angle deviation, the pressing speed, and the forming temperature exhibited negligible effects on the forming results. The material flow in the die rib-grooves was affected by the billet manufacturing deviation, the die manufacturing deviation, and the friction factor to some extent, which in turn affected the underfilling rate and strain homogeneity of the die rib-grooves. Additionally, upon analyzing the effects of uncertainty factors on rib-groove filling and strain homogeneity, this study assessed the contribution rates of each factor to determine the fluctuation ranges for multi-objective robust optimization.

3.1.2 Determination of Responses in Dual-RSM

The contribution rate ρ is adopted to quantitatively measure the importance of a single uncertainty factor to each forming index, expressed as:

$$\rho = SS_I/SS_T. \tag{8}$$

Figure 10 shows the contribution rates of each uncertainty factor to the die rib-groove filling and strain homogeneity. As shown in Figure 10, the forming temperature, the pressing speed, and the draft angle deviation

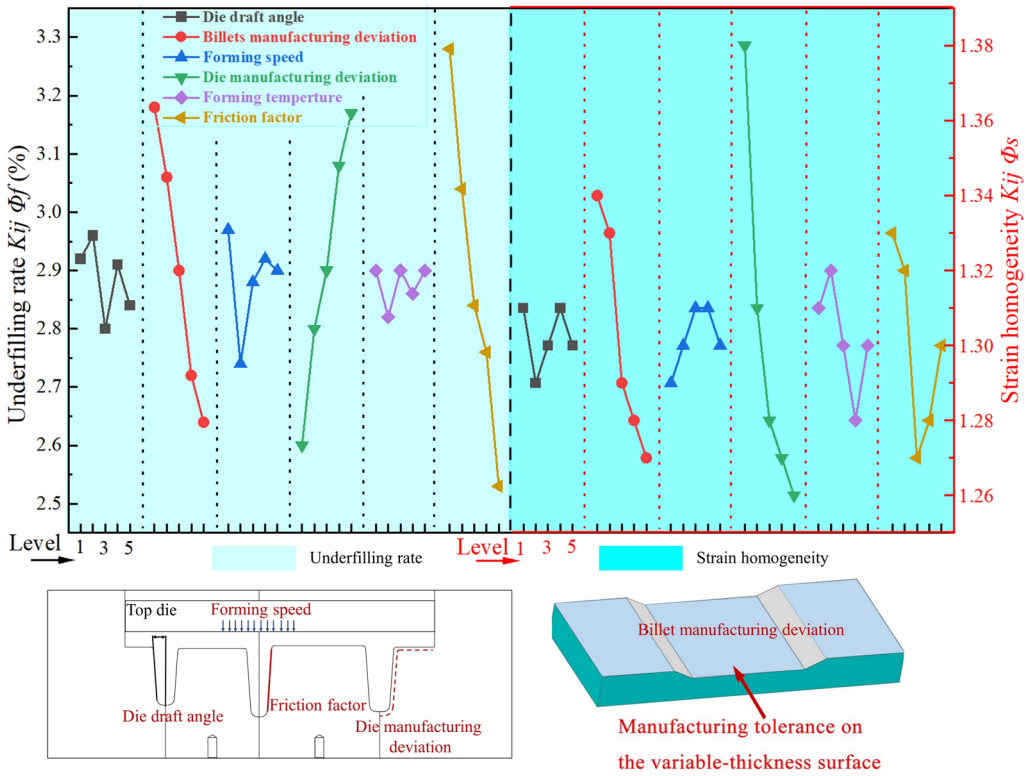

Figure 10 Range analysis results on Φ_f and Φ_s

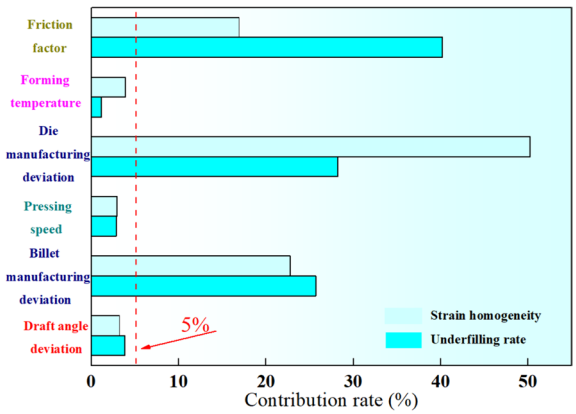

Figure 11 The contribution rate of the fluctuation of uncertainty factors on Φ_f and Φ_s

exhibited little effect on the two objectives, as their contribution rates were < 5%. Accordingly, they were ignored in the billet robust optimization. However, the billet manufacturing deviation, the die manufacturing deviation, and the friction factor exhibited significant effects on the underfilling rate and strain homogeneity. Based on the above studies, the billet manufacturing deviation, the die manufacturing deviation, and the friction factor served as the critical uncertainty factors for the following robust optimization process (Figure 11).

3.2 Design of the Experiment According to BBD Scheme

The level ranges of the deterministic factors and the uncertainty factors are shown in Table 5, where the deterministic factors (*a*, *b*, *c*, and *d*) corresponded to the key size parameters of the UTB. Based on the volume invariance principle, the billet shape was adjusted according to *a*, *b*, *c*, and *d*. The billet was classified into four types of configurations [9], which are shown in Figure 12.

Table 5 The levels of uncertainties and certainties

Factor	Variables	Minimum values	Maximum values
Control factor	a:H_{left}/H_{equal}	0.8	1.2
	b:H_{right}/H_{equal}	0.8	1.2
	c:l_{left}/L_{left}	0.7	0.9
	d:l_{right}/L_{right}	0.7	0.9
Uncontrolled factor	B_{error}	− 0.1	1
	m	0.3	0.5
	M_{error}	-0.1	0.1

Note: H_{equal} is the thickness billet

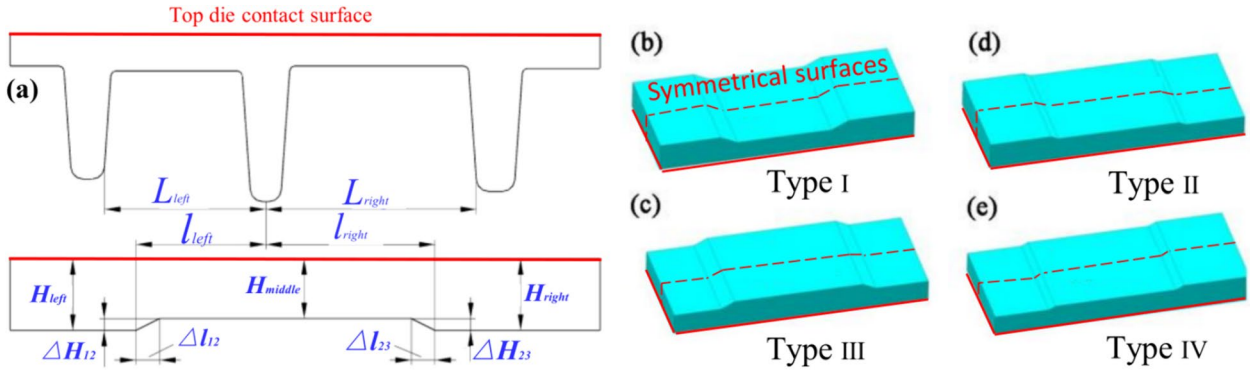

Figure 12 Eigenstructure and four UTB types: (**a**) The geometry parameters of the UTB, (**b**–**e**) Four UTB geometry types

To ensure the reliability of the response surface model, a reasonable experimental design arrangement is inevitable to obtain comprehensive experimental results with fewer experimental runs. Due to the effectiveness of BBD schemes in choosing the experimental factors and level ranges, 29 experiment groups of UTB based on BBD were arranged according to the size parameter combinations outlined in Table 5. The required response objective values were estimated after the FE simulation, as shown in Table 6.

Notably, the average strain represents the average value of the sum of the accumulated strains produced by each element in entire elements. Due to the uncertainty of the initial mesh generation and re-meshing in the FE simulation, mesh sizes in different regions varied, and the number of meshes under different volume distributions also varied. As a result, the strain homogeneity in the table was not efficiently and accurately obtained from the FE simulation results. Gao et al. [41] analyzed the effect of die parameters on the strain inhomogeneity of the local loading transitional region based on the plane strain, considering the area ratio of the mesh. Accordingly, the following indicators were adopted to evaluate the strain inhomogeneity of the component [42, 43]:

$$\varphi_1 = \sum_{i=1}^{N} (\overline{\varepsilon_i} - \overline{\varepsilon}_{ave})^2, \tag{9}$$

$$\varphi_2 = \frac{1}{N} \sum_{i=1}^{N} (\overline{\varepsilon_i} - \overline{\varepsilon}_{ave})^2, \overline{\varepsilon}_{ave} = \sum_{i=1}^{N} \varepsilon_i / N, \tag{10}$$

$$\varphi_3 = \overline{\varepsilon}_{max} - \overline{\varepsilon}_{min}, \tag{11}$$

$$\begin{aligned} \varphi_4 &= \sum_{i=1}^{N} v_i \left(\overline{\varepsilon_i} - \overline{\varepsilon}_{ave}{}' \right)^2 / \sum_{i=1}^{N} v_i, \overline{\varepsilon}_{ave}{}' \\ &= \sum_{i=1}^{N} v_i \overline{\varepsilon}_i / N / \sum_{i=1}^{N} v_i, \end{aligned} \tag{12}$$

where $\overline{\varepsilon_i}$ and v_i are the equivalent strain and volume of element i, respectively. $\overline{\varepsilon}_{max}$ and $\overline{\varepsilon}_{min}$ are the maximum and minimum equivalent strain of element i, respectively.

To ensure the reliability of the strain homogeneity, the influence of uneven mesh size on the symmetric statistical results was eliminated. The average mesh size Φ_s is expressed as:

$$\Phi_s = \sum_{i=1}^{N} v_i \overline{\varepsilon_i} / \sum_{i=1}^{N} v_i, \tag{13}$$

where i is the strain of each element, N is the total number of elements, and v_i is the volume of the ith element.

The specific implementation process is shown in Figure 13. All the strain data by each element was extracted from the Deform-3D simulation. Subsequently, Φs was calculated using the mathematical software.

3.3 Intelligent Modeling Evaluation Based on Dual Response Surface

3.3.1 Establishment of Response Surface Models and Evaluation

(1) Establishing the Response Surface Models:

In the process of establishing the response surface, a quadratic polynomial was used to ensure the accuracy of the model, as shown in Eq. (14):

$$y = \beta_0 + \sum_{ij}^{k=1} \beta_{jj} x_j + \sum_{j}^{k=1} \sum_{j}^{k} \beta_i x_j, \tag{14}$$

where y is the response (a comprehensive index of the underfilling rate of the rib-groove), x_i and x_j are the input variables ($a = H_{left}/H_{equal}$, $b = H_{right}/H_{equal}$, $c = l_{left}/L_{left}$, $d = l_{right}/L_{right}$), k is the number of variables, and β_0, β_i, and β_{ij} are the regression coefficients.

Table 6 The cross array with size parameters of UTB and uncertainty factors

Control factors						Uncertainty factors						Objectives	
						UD	1	2	3	4	5		
The size parameters of the UTB												Mean	SD
	a	*b*	*c*	*d*	H_{middle}	B_{error}	− 0.1	− 0.05	0	0.05	0.1		
						m	0.395	0.405	0.39	0.40	0.415		
						M_{error}	0.05	0	− 0.05	− 0.1	0.1		
The performance of the die underfilling												Φ_f^μ	Φ_f^σ
1	0.8	1.0	0.9	0.8	26.30	7.51%	7.56%	7.70%	8.45%	7.37%		7.71	0.42
2	1.0	1.0	0.8	0.8	24.20	2.71%	2.13%	2.37%	3.26%	1.89%		2.47	0.53
3	1.0	1.2	0.7	0.8	20.65	12.10%	12.83%	11.74%	12.99%	12.82%		12.49	0.25
4	0.8	1.0	0.8	0.9	26.50	8.76%	8.39%	8.83%	9.82%	12.98%		9.75	1.88
5	1.2	1.0	0.8	0.7	21.45	6.60%	7.04%	5.70%	6.46%	9.95%		7.15	1.63
6	1.0	1.0	0.8	0.8	24.20	3.26%	2.09%	3.41%	3.04%	2.37%		2.83	0.57
7	1.0	1.0	0.9	0.9	24.20	3.10%	2.12%	3.39%	3.19%	3.08%		2.97	0.49
8	1.0	0.8	0.8	0.9	26.85	5.22%	11.69%	5.87%	5.77%	6.00%		6.91	2.68
9	1.2	1.0	0.8	0.9	21.85	6.60%	7.54%	6.74%	7.57%	11.65%		8.02	2.08
10	1.0	1.0	0.9	0.7	21.90	5.39%	5.49%	4.72%	5.47%	5.71%		5.35	0.37
11	1.2	1.0	0.9	0.8	22.10	5.45%	6.06%	4.89%	6.05%	6.25%		5.74	0.56
12	1.0	0.8	0.7	0.8	27.75	5.58%	6.26%	5.34%	6.17%	5.74%		5.82	0.39
13	0.8	0.8	0.8	0.8	31.20	5.25%	5.80%	4.55%	5.37%	6.18%		5.43	0.61
14	0.8	1.2	0.8	0.8	23.45	18.14%	18.83%	16.28%	18.74%	19.34%		18.26	1.18
15	1.0	0.8	0.9	0.8	27.30	7.08%	6.61%	6.47%	6.81%	7.07%		6.81	0.27
16	1.0	1.0	0.8	0.8	24.20	2.89%	2.26%	3.18%	3.22%	2.31%		2.77	0.46
17	1.0	1.2	0.9	0.8	21.10	12.72%	13.36%	12.62%	12.92%	12.98%		12.92	0.28
18	0.8	1.0	0.7	0.8	27.25	9.16%	8.77%	9.15%	9.42%	8.30%		8.96	0.43
19	1.2	1.2	0.8	0.8	17.20	8.87%	9.85%	8.52%	9.86%	9.90%		9.39	0.65
20	1.0	0.8	0.8	0.7	28.30	7.53%	7.20%	7.28%	7.43%	6.93%		7.27	0.23
21	0.8	1.0	0.8	0.7	26.95	8.07%	7.25%	8.31%	8.94%	7.43%		8.00	0.68
22	1.0	1.0	0.8	0.8	24.20	3.40%	2.74%	3.44%	3.24%	2.33%		3.03	0.48
23	1.2	0.8	0.8	0.8	24.95	12.76%	13.15%	18.15%	13.33%	13.75%		14.22	2.22
24	1.0	1.0	0.7	0.9	24.20	2.87%	2.53%	3.11%	3.55%	5.32%		3.47	1.09
25	1.0	1.0	0.7	0.7	24.20	2.53%	2.18%	2.90%	3.06%	2.63%		2.66	0.34
26	1.2	1.0	0.7	0.8	21.15	8.20%	8.40%	7.11%	8.55%	8.83%		8.22	0.66
27	1.0	1.2	0.8	0.9	21.55	11.24%	10.98%	10.29%	11.63%	11.37%		11.10	0.51
28	1.0	1.0	0.8	0.8	24.20	3.45%	2.74%	3.13%	3.04%	2.18%		2.91	0.48
29	1.0	1.2	0.8	0.7	20.10	14.26%	14.73%	13.79%	17.23%	15.16%		15.03	1.33
The performance of the average strain												Φ_s^μ	Φ_s^σ
1	0.8	1.0	0.9	0.8	26.30	1.487	1.327	1.307	1.311	1.318		1.350	0.076
2	1.0	1.0	0.8	0.8	24.20	1.261	1.188	1.129	1.094	1.13		1.160	0.065
3	1.0	1.2	0.7	0.8	20.65	1.313	1.397	1.487	1.202	1.398		1.359	0.107
4	0.8	1.0	0.8	0.9	26.50	1.276	1.376	1.272	1.2882	1.356		1.314	0.048
5	1.2	1.0	0.8	0.7	21.45	1.178	1.178	1.135	1.173	1.220		1.177	0.030
6	1.0	1.0	0.8	0.8	24.20	1.209	1.353	1.181	1.202	1.265		1.242	0.069
7	1.0	1.0	0.9	0.9	24.20	1.098	1.141	1.094	1.189	1.172		1.139	0.042
8	1.0	0.8	0.8	0.9	26.85	1.343	1.370	1.492	1.296	1.352		1.371	0.073
9	1.2	1.0	0.8	0.9	21.85	1.163	1.225	1.165	1.125	1.414		1.218	0.115
10	1.0	1.0	0.9	0.7	21.90	1.165	1.219	1.140	1.155	1.264		1.188	0.051
11	1.2	1.0	0.9	0.8	22.10	1.166	1.207	1.138	1.146	1.218		1.175	0.035

Table 6 (continued)

The performance of the average strain											Φ_s^{μ}	Φ_s^{σ}
12	1.0	0.8	0.7	0.8	27.75	1.292	1.368	1.258	1.312	1.329	1.312	0.041
13	0.8	0.8	0.8	0.8	31.20	1.500	1.586	1.488	1.518	1.596	1.537	0.049
14	0.8	1.2	0.8	0.8	23.45	1.620	1.593	1.443	1.628	1.683	1.593	0.090
15	1.0	0.8	0.9	0.8	27.30	1.307	1.326	1.278	1.449	1.374	1.347	0.067
16	1.0	1.0	0.8	0.8	24.20	1.114	1.138	1.086	1.182	1.173	1.139	0.046
17	1.0	1.2	0.9	0.8	21.10	1.316	1.386	1.297	1.38	1.380	1.352	0.041
18	0.8	1.0	0.7	0.8	27.25	1.592	1.403	1.291	1.305	1.398	1.398	0.120
19	1.2	1.2	0.8	0.8	17.20	1.360	1.371	1.342	1.321	1.453	1.369	0.050
20	1.0	0.8	0.8	0.7	28.30	1.266	1.326	1.291	1.286	1.397	1.313	0.051
21	0.8	1.0	0.8	0.7	26.95	1.612	1.383	1.360	1.385	1.611	1.470	0.129
22	1.0	1.0	0.8	0.8	24.20	1.170	1.151	1.016	1.189	1.161	1.138	0.069
23	1.2	0.8	0.8	0.8	24.95	1.297	1.356	1.313	1.283	1.391	1.328	0.044
24	1.0	1.0	0.7	0.9	24.20	1.104	1.163	0.913	1.105	1.244	1.106	0.122
25	1.0	1.0	0.7	0.7	24.20	1.094	1.136	1.087	1.095	1.162	1.115	0.032
26	1.2	1.0	0.7	0.8	21.15	1.188	1.136	1.162	1.162	1.241	1.178	0.040
27	1.0	1.2	0.8	0.9	21.55	1.507	1.324	1.256	1.215	1.332	1.327	0.112
28	1.0	1.0	0.8	0.8	24.20	1.213	1.251	1.088	1.202	1.261	1.203	0.069
29	1.0	1.2	0.8	0.7	20.10	1.334	1.427	1.433	1.452	1.425	1.414	0.046

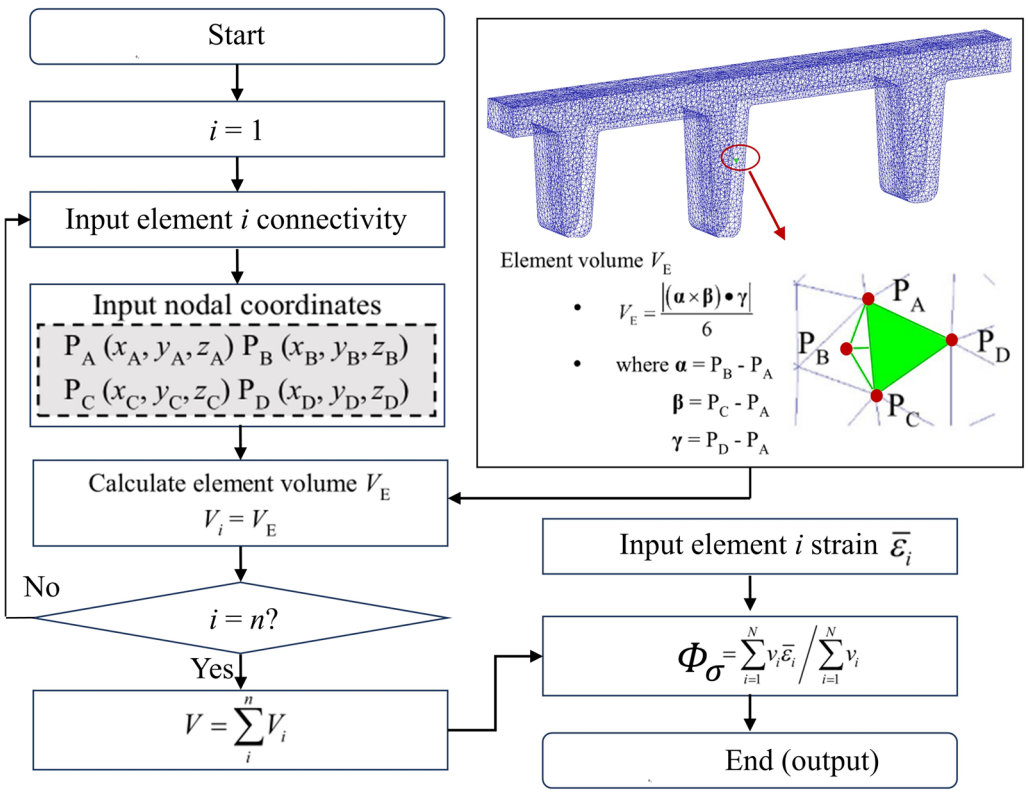

Figure 13 Flow chart for volume and Φ_s calculation in Deform-3D simulation

According to the calculated results in Table 6, the response surface models obtained using the stepwise regression method are shown as follows.

$$\begin{aligned}\Phi_f^{\mu} =& 128.18 - 72.03a - 129.97b - 5.83432c \\ & - 66.56595d - 99.57853ab - 15.43701ac \\ & - 11.07973ad - 7.06185bc - 44.62635b \\ & - 79.84940cd + 95.65503a^2 + 141.91240b^2 \\ & + 57.57730c^2 + 114.65848d^2,\end{aligned} \tag{15}$$

$$\begin{aligned}\Phi_f^{\sigma} =& -39.97610a + 34.55824b + 77.55935c \\ & - 20.00825d - 9.45457ab - 1.12854ac \\ & - 9.41639ad - 1.74976bc - 40.96317bd \\ & - 15.79403cd + 10.60585a^2 + 4.00818b^2 \\ & - 39.32813c^2 + 54.04943d^2,\end{aligned} \tag{16}$$

$$\begin{aligned}\Phi_s^{\mu} =& 7.18316 - 8.59824a - 6.91347b \\ & + 4.27353c + 0.72624d - 0.090709ab \\ & + 0.56761ac + 2.48009ad - 0.52831bc \\ & - 1.81069bd - 1.02631cd + 2.87186a^2 \\ & + 4.48082b^2 - 2.13870c^2 - 0.46531d^2,\end{aligned} \tag{17}$$

$$\begin{aligned}\Phi_s^{\sigma} =& 0.45635 - 2.54039a + 0.73700b \\ & + 2.49291c - 1.21580d - 0.21477ab \\ & + 0.48913ac + 2.81980ad - 1.14320bc \\ & + 0.55295bd - 2.45313cd.\end{aligned} \tag{18}$$

(2) Evaluation of the Response Surface Models:

In this study, RSM not only reduced the number of experiments but also comprehensively analyzed the influence of various factors on the response value, including their interactions. The last term in Eq. (14) represents the interaction between factors [44]. To assess the reliability of the model, it was essential to analyze the regression equation and coefficients after establishing the response surface model. The simulation results in Table 6 underwent variance analysis. The analysis of variance (ANOVA) results of the mean and variance of the underfilling rate and the mean and variance of the strain homogeneity are shown in Table 7, respectively. The statistical significance was tested using F-value and P-value. The F-value is the ratio of the mean square of the effect and the mean square of the error, which reflects the magnitude of the random error. The P-value is a parameter used to evaluate the result of the hypothesis testing. The smaller the P-value, the more significant the result. Also, the closer the adjusted coefficient of multiple determination R^2 is to 1, the better the model fits the data.

Table 7 shows the ANOVA table of the response surface model for the mean and variance. It was evident that the significance probability P of the model was < 0.0001, indicating that the model was extremely significant ($P < 0.01$). Upon analyzing the test value of the lack-of-fit term, it was evident that the lack-of-fit term was not significant and the constructed regression model was valid. The R^2 of the model was > 0.9, indicating an excellent predictive ability of the model. The adjusted R^2 was > 0.9,

Table 7 The ANOVA of dual-RSM

	F-Value				p-value (Prob > F)				
	Φ_f^{μ}	Φ_f^{σ}	Φ_s^{μ}	Φ_s^{σ}	Φ_f^{μ}	Φ_f^{σ}	Φ_s^{μ}	Φ_s^{σ}	
Model	20.19	21.72	29.85	27.10	<0.0001	<0.0001	<0.0001	<0.0001	Significant
AB	47.86	30.07	0.049	2.59	<0.0001	<0.0001	0.8273	0.1248	
AC	0.23	0.054	0.48	3.36	0.6360	0.8203	0.4980	0.0833	
AD	0.12	3.73	9.24	111.73	0.7336	0.0740	0.0088	<0.0001	
BC	0.049	0.13	0.28	14.23	0.8281	0.7251	0.6079	0.0014	
BD	1.96	70.57	4.92	4.30	0.1837	<0.0001	0.0435	0.0528	
CD	1.57	2.62	0.26	15.84	0.2314	0.1276	0.6205	0.0009	
Lack of Fit	51.61	25.39	0.33	1.18	0.90	0.35	0.9249	0.4808	Not significant
R^2	0.9528	0.9560	0.9676	0.9487					
Adj R^2	0.9056	0.9120	0.9352	0.9231					

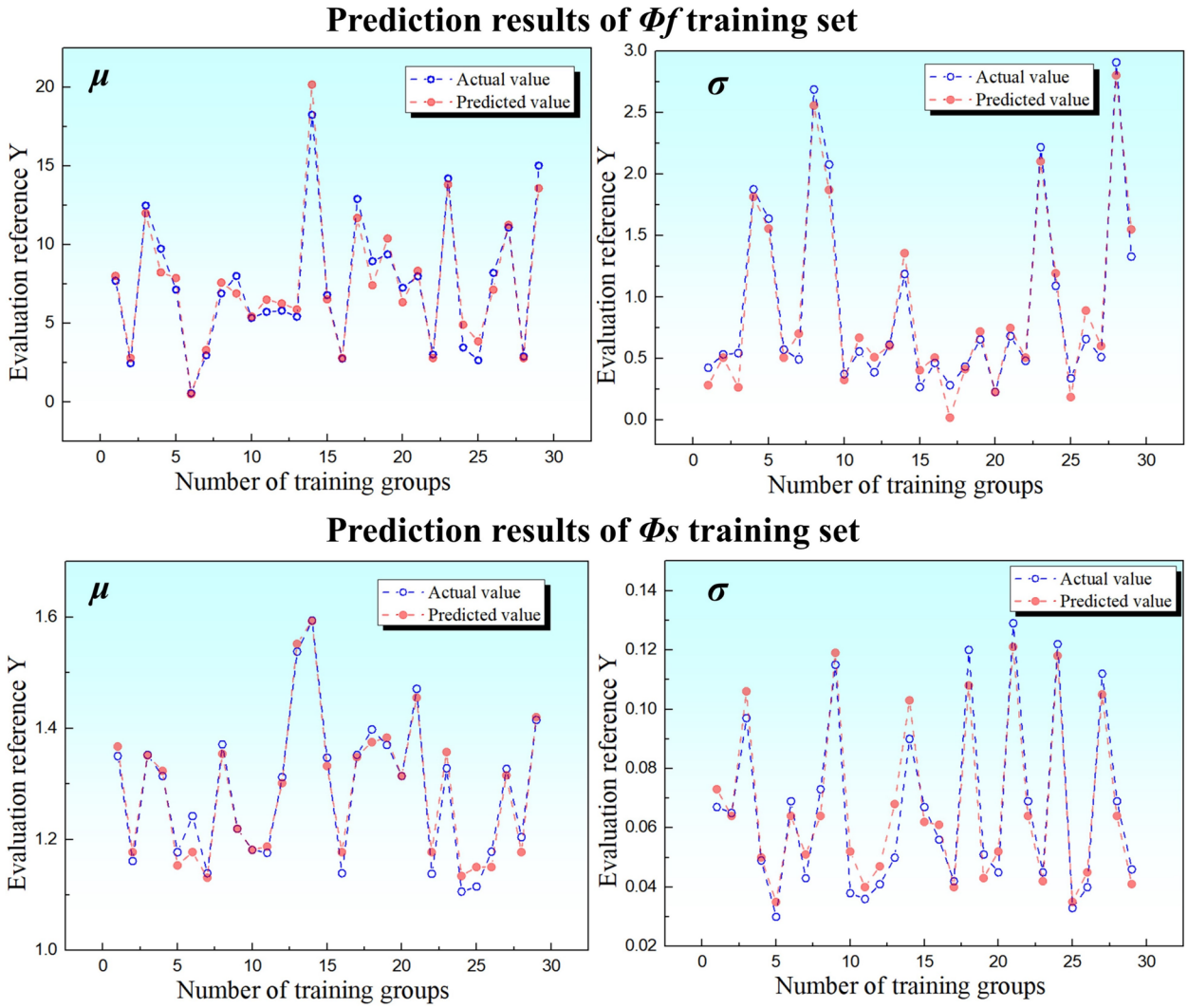

Figure 14 Distribution of the actual and predicted values of Φ_f and Φ_s

Table 8 Eight experiments by the random selection for verification of the dual-RSM

Scheme No.	*a*	*b*	*c*	*d*	*Pre-*Φ_f^{μ}	*Actual-*Φ_f^{μ}	*Pre-*Φ_f^{σ}	*Actual-*Φ_f^{σ}	*Pre-*Φ_s^{μ}	*Actual-*Φ_s^{μ}	*Pre-*Φ_s^{σ}	*Actual-*Φ_s^{σ}
1	0.88	1.03	0.8	0.75	5.65%	5.23%	3.01	2.09	1.321	1.329	0.086	0.93
2	1.13	1.15	0.84	0.79	7.52%	5.74%	2.41	2.95	1.282	1.276	0.039	0.043
3	1.05	1.08	0.72	0.84	5.15%	3.42%	0.54	0.88	1.180	1.124	0.101	0.093
4	1.19	1.06	0.78	0.855	6.23%	4.27%	4.10	3.12	1.221	1.213	0.091	0.082
5	1.04	0.82	0.715	0.875	6.77%	4.26%	2.38	2.75	1.293	1.343	0.075	0.87
6	1.08	1.19	0.9	0.85	8.95%	7.29%	1.29	0.99	1.299	1.297	0.046	0.065
7	0.86	1.12	0.83	0.71	11.9%	10.41%	3.35	2.66	1.451	1.457	0.098	0.105
8	0.97	0.85	0.895	0.73	5.18%	3.34%	3.07	2.93	1.288	1.262	0.077	0.078

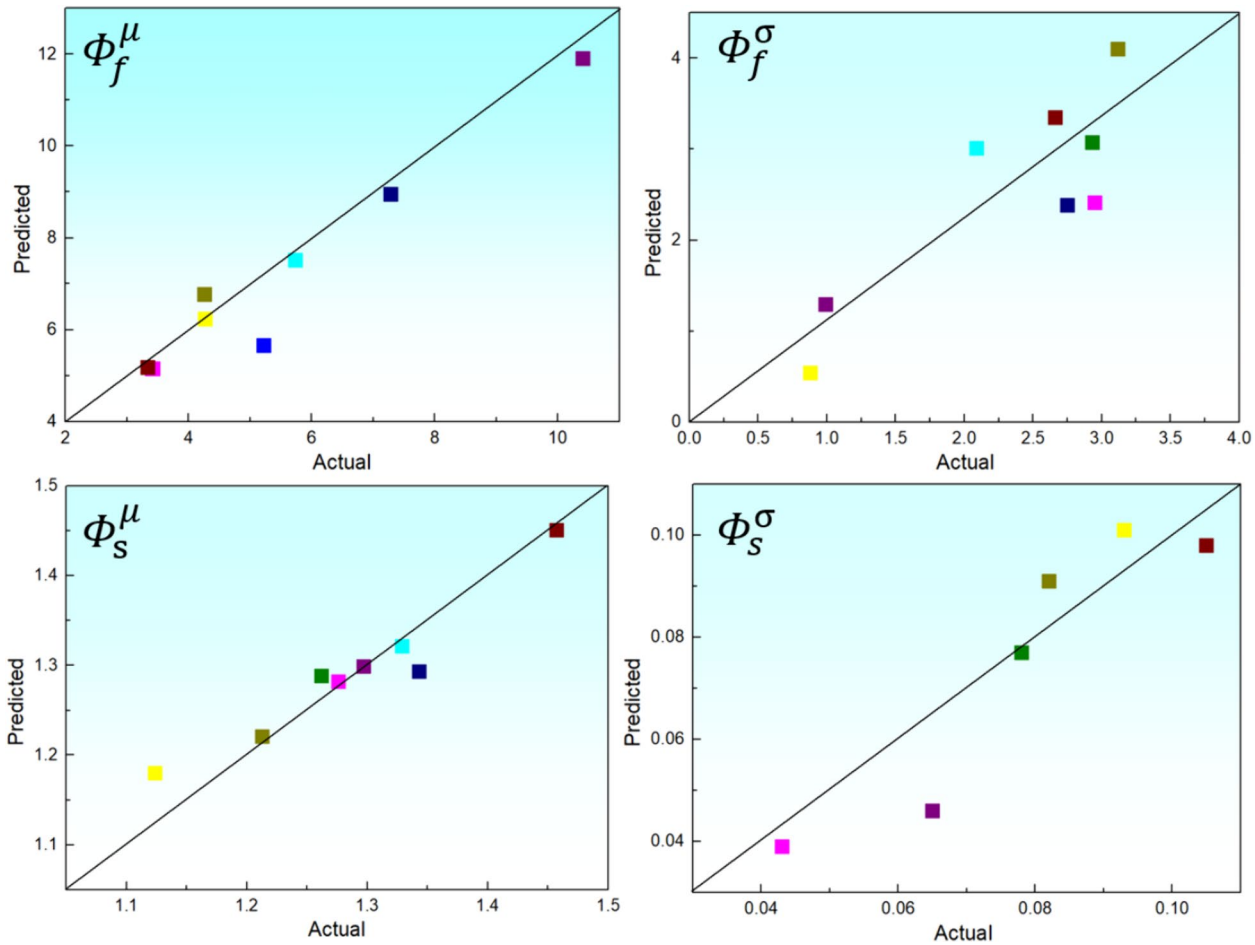

Figure 15 8 experiments by the random selection between simulated values and predicted values: **a** Φ_f^μ, **b** Φ_f^σ, **c** Φ_s^μ, **d** Φ_s^σ

implying an excellent fit for the regression model. Meanwhile, the model terms *AB* and *BD* were significant in the underfilling rate, indicating that the comprehensive adjustment of the key size parameters of the billet exhibited a significant impact on the rib-groove filling. Furthermore, the model terms *A*, *AD*, *BC*, *CD*, A^2, and B^2 were significant in the strain homogeneity, which indicated that the selected key parameters exhibited a significant impact on the strain homogeneity.

Figure 14 shows the distribution of the actual values and the predicted values. All the points of the actual value parameters were approximately distributed along the points of the predicted value parameters. The prediction results indicated that the accuracy of the prediction model of the die rib-groove filling and strain homogeneity established using the training samples was consistent with the ANOVA results. Thus, indicating that the predicted values of the model were consistent with the actual values. The quadratic regression equation fitted by the model was used for further optimization. Moreover, eight experiments via random selection were conducted to assess the accuracy of the dual-RSM.

From the analysis of Table 8, it was observed that the error of the random experiment results was small. From the perspective of die rib-groove filling, the error between the actual value and the predicted value was small, as the maximum error of the mean reached 2.51% and the maximum error of the variance reached 0.98%, respectively. From the perspective of strain homogeneity, the error between the actual value and the predicted value was significantly small, as the maximum error of the mean reached 0.050, and the maximum error of the variance reached 0.019, respectively. Figure 15 presents the comparison with the actual and predicted values. This further indicated that the correlation of the rib-groove filling and strain homogeneity with the UTB size parameters was effective and reliable, enabling the FE simulation to quickly calculate the

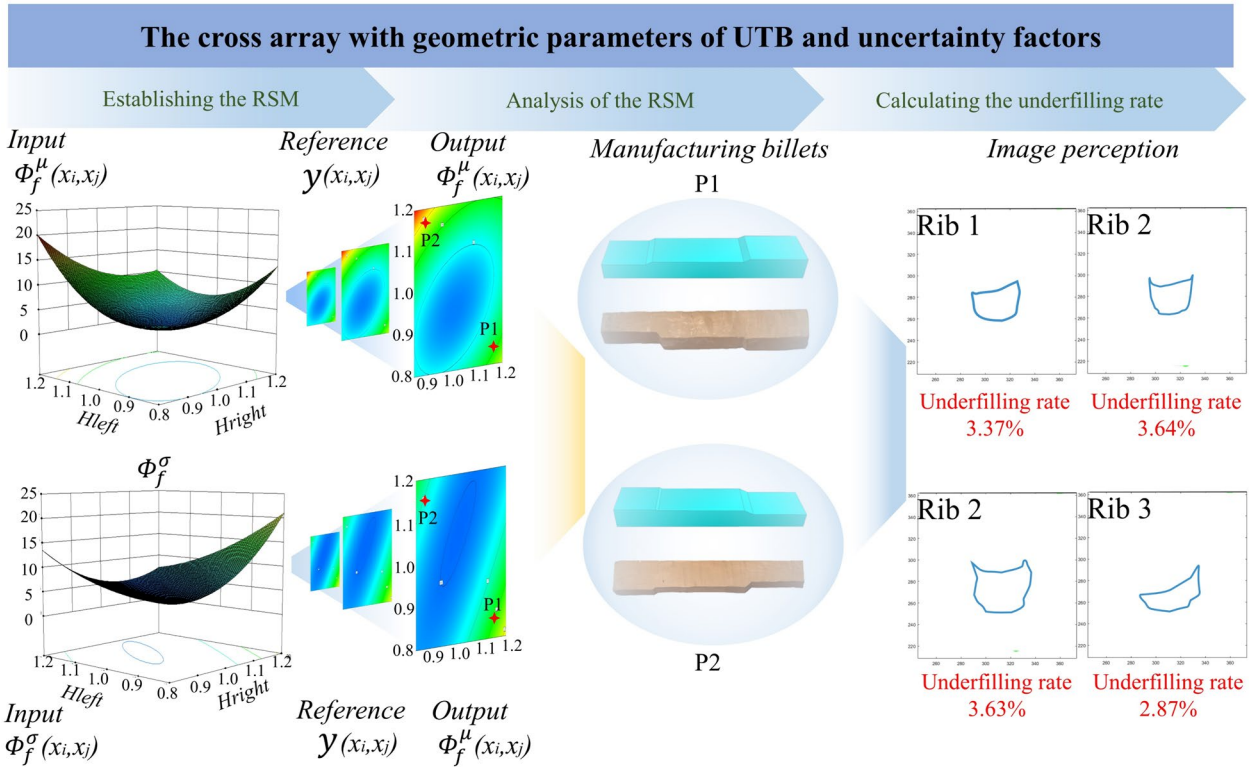

Figure 16 The dual-RSM of underfilling rate; **a** Φ^{μ}; **b** Φ^{σ}

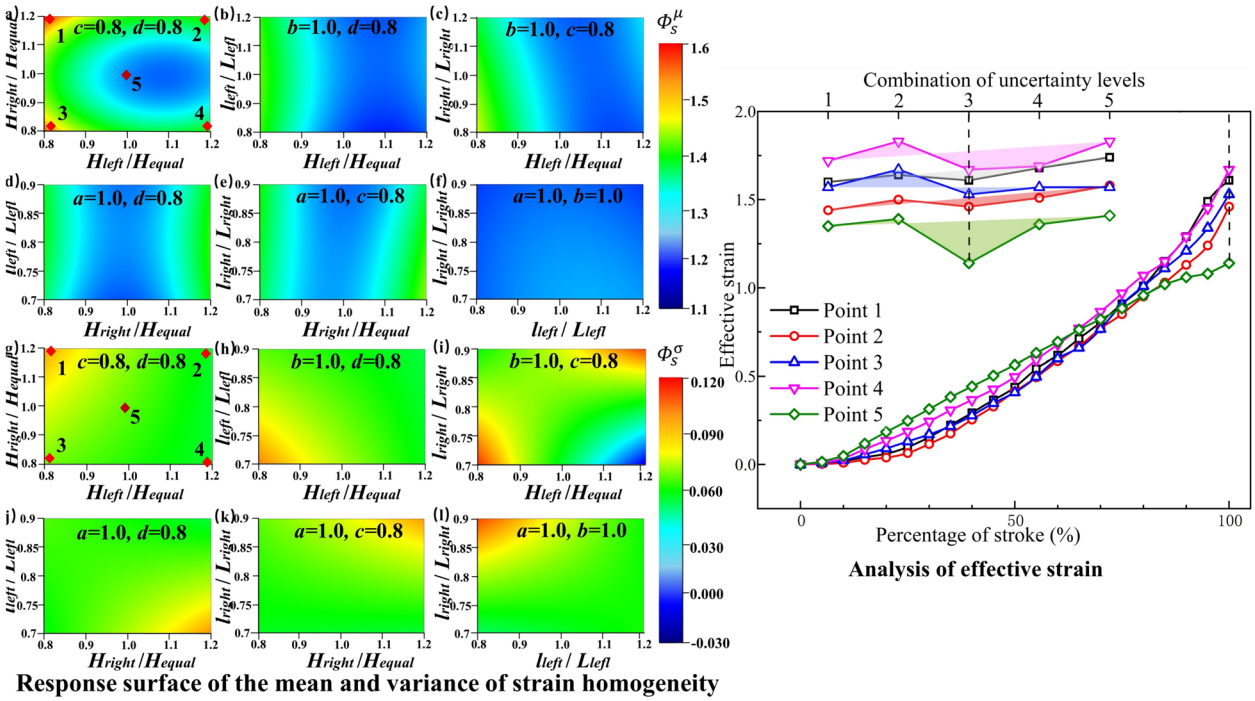

Figure 17 The variation of H_{right} and H_{left} on average strain based on dual-RSM

rib-groove filling and strain homogeneity for the UTB with different size parameters.

3.3.2 Interaction of Key Factors on Rib-grooves Filling

From Eqs. (15) and (16), it was observed that the interaction of *a, b, c*, and d exhibited an influence on the rib-groove filling. According to ANOVA in Tables 7 and 8, compared with other key size parameters, the interaction of *a* and *b* exhibited a more significant influence on the rib-groove filling. The interaction response surface three-dimensional plots are drawn according to Eqs. (15) and (16), as shown in Figure 16. Under the fluctuation of uncertainty factors and the interaction of *a* and *b*, with the increase of H_{left} and H_{right}, the mean and variance of the underfilling rate exhibited a trend of decreasing and then increasing. Thus, as the H_{right} increased, the first fully-filled rib-groove switched from Rib 1 to Rib 3.

After the image perception processing and analysis of the rib-groove monitoring, the die underfilling rate of the UTB utilizing point 1 and point 2 were 7.01% and 6.50%, respectively. The results of PSE further indicated that the interaction between *a* and *b* exhibited a significant effect on the filling of the groove. Further optimization of the response surface model was needed.

3.3.3 Interaction of Key Factors on Strain Homogeneity

Furthermore, Figure 17 represents the variation of H_{right} and H_{left} on the average strain, the four types of UTB variations are shown in Figure 12. Hence, the strain homogeneity of the components was regulated and optimized by altering the UTBs with different size parameters.

It can derived from Eqs. (17) and (18) that the strain homogeneity of the component was affected by the interaction of *a, b, c*, and d. Figure 17 shows that *a* and *b* exhibited a greater influence on the strain homogeneity. The mean index of strain homogeneity initially declined and then rose with increased H_{right} and H_{left} from a low level. The fluctuation ranges of strain homogeneity increased slightly with increased H_{right}.

3.4 Multi-objective Intelligent Decision Making Based on NSGA-II

In this study, the multi-objective optimization of the Ti-alloy multi-rib eigenstructure was essentially dependent on billet optimization. The optimal solution was utilized to adjust the key size parameters of the UTB based on modeling and solving.

In practical engineering applications, multiple objectives need to be defined and optimized. However, the

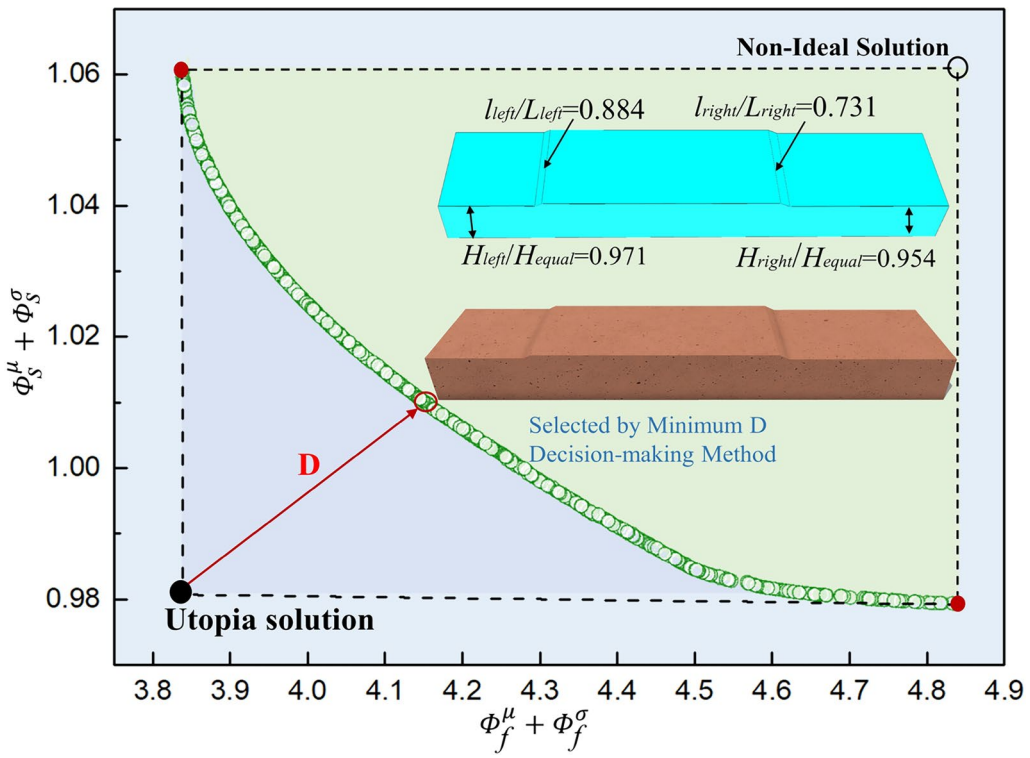

Figure 18 The solution set of the UTBs by NSGA-II

optimal solutions for each objective were often not achieved in the optimization process. To address the multi-objective optimization problems, multiple related parameters and indicators were considered comprehensively [45, 46]. Based on the dual-RSM of rib-groove filling and strain homogeneity, a multi-objective robust optimization model for titanium alloy multi-rib eigenstructure was established. Because the optimization objectives involve two response functions of mean and variance, the approach added mean and variance, representing the optimization variable function. The objective functions f_1 and f_2 were optimally maximized within the range of the independent variables, requiring that the values of both f_1 and f_2 were minimized simultaneously. Finally, the multi-objective robust optimization problem was transformed into solving the optimization model, as shown in Eq. (19):

$$\begin{aligned}
&\text{Find or variables}: a.b.c.d\\
&\text{Minimize}: f_1(a,\ b,\ c,\ d) f_2(a,b,c,\ d)\\
&\left(\Phi_{\mathrm{f}}^{\sigma}+\Phi_{\mathrm{f}}^{\mu},\ \Phi_{\mathrm{s}}^{\sigma}+\Phi_{\mathrm{s}}^{\mu}\right)\\
&\text{Subject to constraints}:\\
&V_{UTB}(a,\ b,\ c,\ d)\ =\mathrm{V}_{\mathrm{eigen}}\\
&\text{With in ranges}:\\
&0.8\le a\le 1.2 \quad 0.8\le b\le 1.2\\
&0.7\le c\le 0.9 \quad 0.7\le d\le 0.9
\end{aligned} \tag{19}$$

Generally, the solution methods for multi-objective optimization problems can be divided into two categories. One is to transform the multi-objective problem into a single objective using weighting or constraint methods. The other is to construct a non-dominated solution set based on improved algorithms, and then obtain the Pareto solution by approaching the optimal solution through the solution set. A widely used method is the non-dominated sorting algorithm with an elitism strategy (NSGA-II) [47, 48]. This study adopted the multi-objective optimization algorithm based on NSGA-II, with a crossover probability of 0.9, the maximum number of iterations was 200, and the population size was 100. The multi-objective optimization was solved using MATLAB software. The solution set is obtained and illustrated in Figure 18. The *X*-axis shows the sum of the mean and variance of the underfilling rate, while the *Y*-axis shows the sum of the mean and variance of the strain homogeneity. Generally, the multi-objective optimization solution was not unique, owing to a set of balanced solutions called the Parato-optimal front. The green circles in the middle revealed the Pareto frontier of dual-objective optimization using NSGA-II. Any solution in this set of solutions is better than the solutions in other regions, thus each point on the frontier reached the optimal solution. Nevertheless, there was a conflict and constraint between the two objectives, enabling the multi-objective optimization solution unable to reach the optimal solution of the single-objective optimization. Therefore, it was difficult to achieve desirable die-groove filling and strain homogeneity simultaneously to a maximum extent.

For multi-objective optimization problems, the goal is to find the best solution that optimizes multiple conflicting objectives simultaneously. However, all solutions on the Pareto frontier are non-dominated, which can be chosen as the optimal solutions. The solutions that achieved the excellent trade-off between these objectives were known as Pareto-optimal solutions. The minimum distance method enabled all the objectives to be satisfied in the multi-objective optimization. It was employed to select the optimal solution, balancing, and constraining each other from the Pareto solution set. This method not only enhanced die-groove-filling but also improved the strain homogeneity of the component. The minimum distance method is expressed as follows.

$$\mathrm{Min}\,D=\sqrt{\sum_{\tau=1}^{U}(f_{\tau}-f_{\tau}^{utopia})^2}, \tag{20}$$

where U denotes the number of objectives, τ is an individual solution in the Pareto solution set, f_{τ}^{utopia} is the single-objective optimal solution.

To reflect the numerical magnitude of the two objectives clearly, the normalization with a dimensionless value between 0 and 1 was adopted and the normalized value is expressed as:

$$\Phi f^{*}(p)=\frac{\Phi f(p)-\min[\Phi f(p)]}{\max[\Phi f(p)]-\min[\Phi f(p)]}, \tag{21}$$

$$\Phi \mathrm{s}^{*}(p)=\frac{\Phi s(p)-\min[\Phi s(p)]}{\max[\Phi s(p)]-\min[\Phi s(p)]}, \tag{22}$$

where $\Phi f(p)$ is the underfilling rate of the Pth experiment, $\max[\Phi f(p)]$ and $\min[\Phi f(p)]$ are respective maximum and minimum values of the underfilling rate; $\Phi s(p)$is the strain homogeneity of the Pth experiment; $\max[\Phi s(p)]$and $\min[\Phi s(p)]$ are the maximum and minimum values of the strain homogeneity. Furthermore, combining Min D and normalization, the optimized UTB with desirable die-groove filling and excellent strain homogeneity was obtained, which was the final` optimal solution for the multi-objective robust optimization of Ti-alloy multi-rib eigenstructure. Therefore, Figure 18 shows the Pareto chart of the filling and strain homogeneity of the die rib-grooves filling. The key size parameters of UTB are $a = 0.971$, $b = 0.954$, $c = 0.884$, and $d = 0.731$.

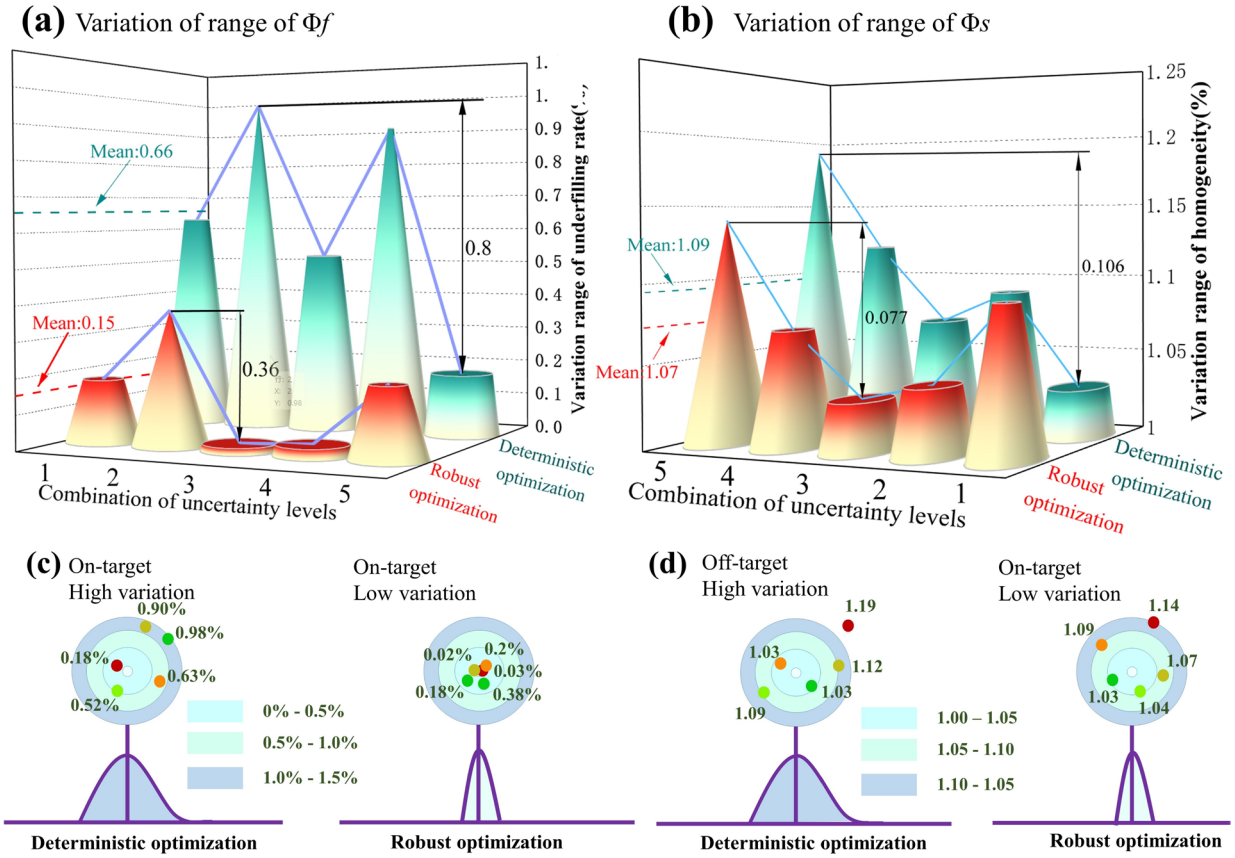

Figure 19 Comparison between the robust and deterministic optimization: **a** variation range of Φ_f; **b** variation range of Φ_s

4 Robust Optimization Results Verification

To further validate the robust optimization effectiveness of the UTB, the deterministic optimization of the UTB, which does not consider the influence of uncertainty factors, was adopted. This allows for comparing the two groups of different optimization solutions. Five groups were selected based on a uniform experimental design from Table 6. For ease of comparison, two objectives were normalized using Eqs. (21) and (22). From Figure 19, the comparison between deterministic optimization

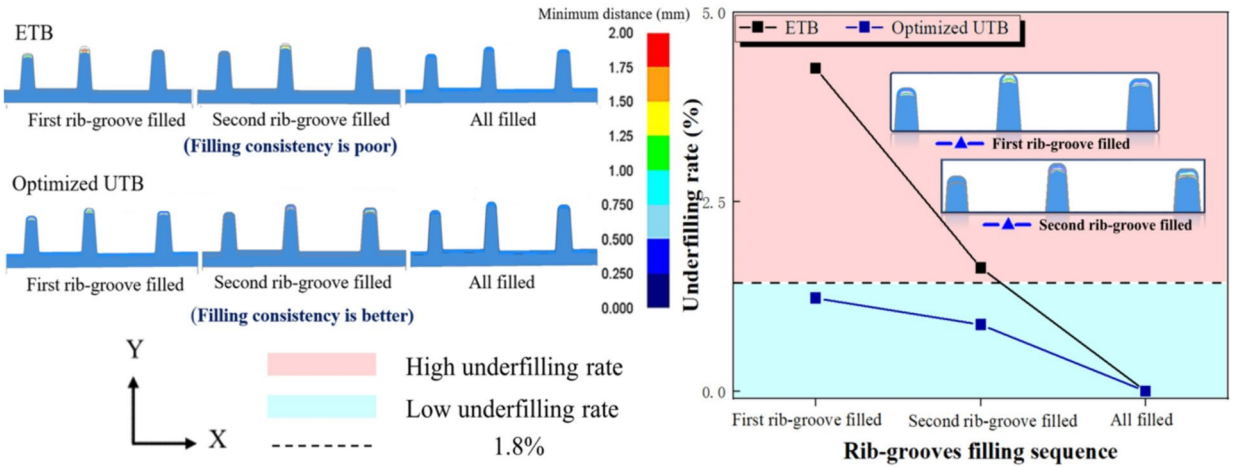

Figure 20 Minimum distance analysis of ETB without optimization and UTB robust optimization

and robust optimization shows a reduction in underfilling rate fluctuation from 0.66 to 0.15 and a decrease in strain homogeneity fluctuation from 1.156 to 1.120. The comparison in Figure 19 indicated that the mean and fluctuation range obtained through robust optimization were both smaller than those of deterministic optimization. This suggests that multi-objective robust optimization is significantly more effective than deterministic optimization.

Furthermore, a minimum distance analysis of the rib-groove filling by UTB robust optimization and ETB without optimization is shown in Figure 20. It was observed from Figure 20 that ETB was initially filled by Rib1 at 95.74%, then by Rib2 at 98.37%, and finally by Rib3 at 100%, indicating a relatively high underfilling rate. According to Figure 19, regardless of which rib was filled, the underfilling rate of the optimized UTB was much lower than that of ETB. The filling of different rib-grooves occurred almost simultaneously at the final moment.

Furthermore, IAPF technology was adopted to track the die-filling status in real-time during the forming

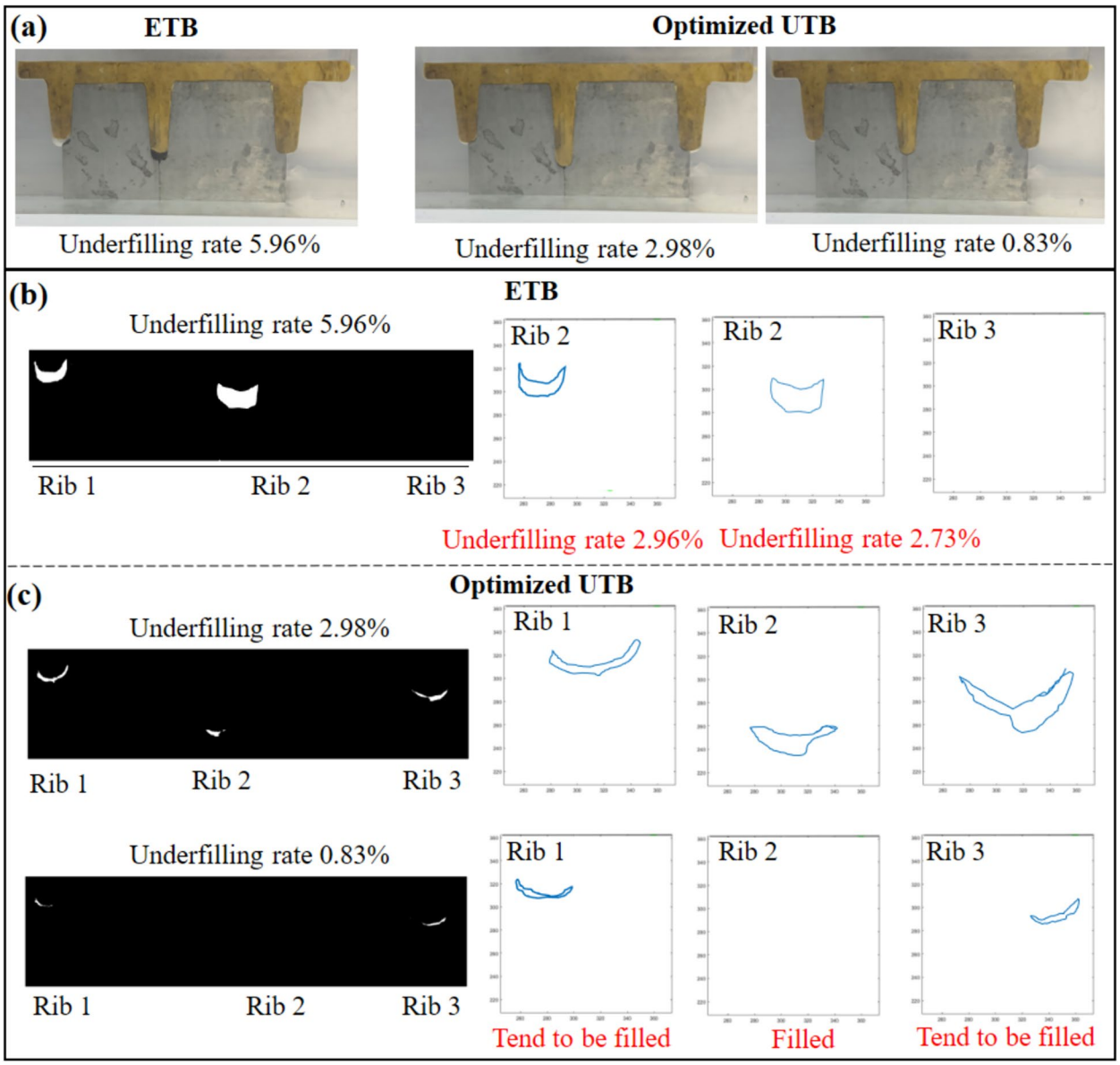

Figure 21 Real-time monitoring of forming process: **a** Filling status before and after optimization, **b** Real-time monitoring of ETB, **c** Real-time monitoring of UTB

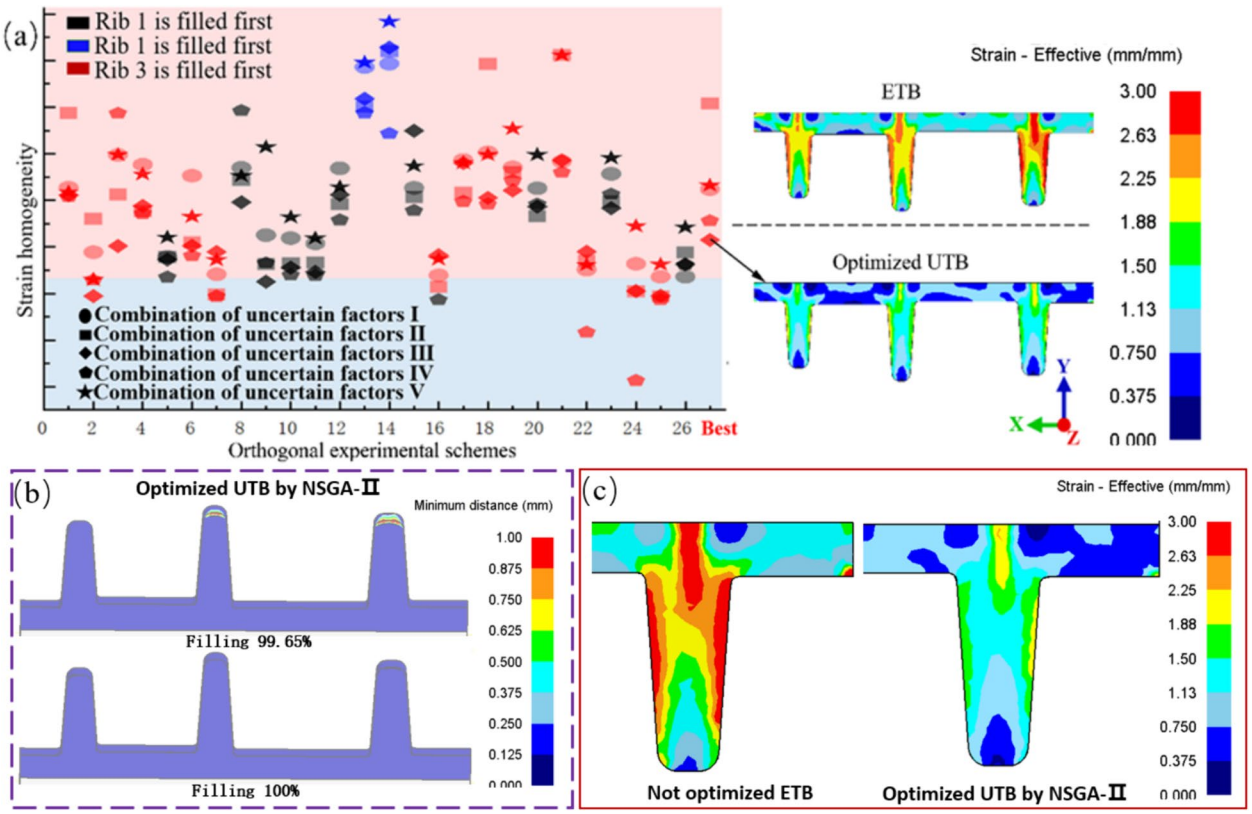

Figure 22 Analysis of deformation uniformity results: **a** The relationship between the cross array and *Φs*, **b** Underfilling rate of optimized UTB, **c** Comparison of strain inhomogeneity

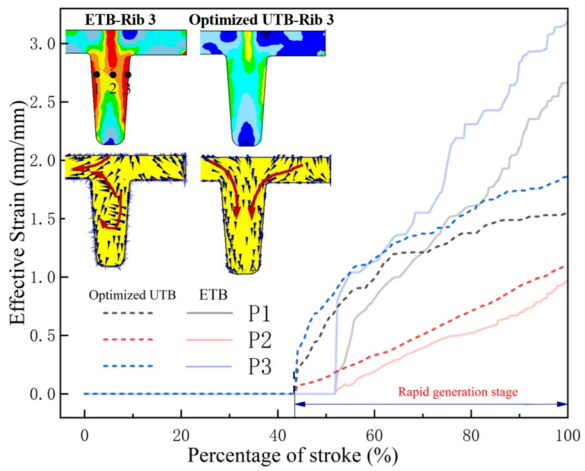

Figure 23 Effective strain analysis based on point tracking

process, without removing it from the die. This verifies the optimization results with PSE based on deterministic and robust optimization solutions. Figure 21 shows that Rib3 was the first rib-groove fully-filled in the forming process by the ETB, with an underfilling rate of 5.69%. It also captured underfilling rates of 2.96% for Rib1 and 2.73% for Rib2. In Figure 21, the underfilling rate of the UTB was significantly improved. When Rib2 was filled first, the underfilling rate was only 0.83%, much smaller than that of the ETB. Meanwhile, the captured underfilling rates of Rib1 and Rib3 were negligible. Therefore, the physical simulation results were consistent with the simulation results. The robust optimized UTB improved the rib-groove filling for the Ti-alloy multi-rib eigenstructure and mitigated the influence of uncertainty factors, enabling the achievement of the most robust rib-groove filling.

However, the strain homogeneity of the component after robust optimization was improved. As shown in Figure 22, the fluctuation results of five uncertainty factors by the optimized UTB were significantly better than those of the 29 groups of billet sizes in Table 6 under the influence of uncertainty. The average strain analysis indicated that Rib3 exhibited a high level of strain with ETB outcomes, and the other two ribs also experienced considerable strain. Alternatively, the strain on the three ribs decreased significantly with optimized UTB outcomes, with Rib1 demonstrating remarkable improvement. It was observed that in the forming process of the ETB,

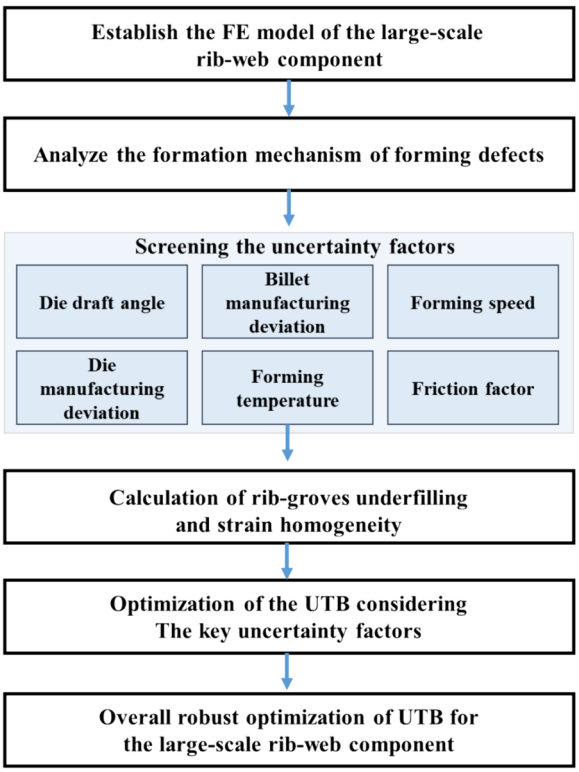

Figure 24 Large-scale rib-web components forming instruction flow chart

as the top die continues to stroke, Rib1 was first filled, resulting in material cross-flow at the web, as shown in Figure 22b. At that moment, the material from the rib1 groove flew back to other rib-grooves, resulting in a significant strain generation. However, the optimized UTB achieved a reasonable volume distribution, minimizing material cross-flow at the web and material backflow in the rib-grooves. Therefore, these significantly mitigated the local strain concentration phenomenon, as shown in Figures 22b and 23c.

Figure 23 further analyzes the strain variation between ETB and the optimized billet. Using the point tracking method, the equivalent strain change process of three positions in rib-groove was obtained. The equivalent strain of three positions increases during the strain increased stage, with positions 1 and 3 in ETB presenting a significant increasing trend, indicating desirable strain homogeneity of the optimized billet.

To attain the preferable rib-groove filling and strain homogeneity in the isothermal forging of titanium alloy multi-rib components.

Firstly, Sun et al. [30] and Wei et al. [9] use simplified models to discuss large-scale components. The region far away from the transitional region can be considered as the whole loading state during the ILLF process. In view of this, the simplified model can reflect the detailed forming characteristics of the transitional region and the corresponding simulation time can be greatly reduced, especially in the 3D FE simulation. In addition, the expense of the experiment can be reduced significantly by using the simplified model.

Secondly, based on the simplified model, the material flow and strain distribution can be easily explored and observed. Then, the uncertain factors that have a great influence on the forming of the component are screened out and used in the later multi-objective robust optimization.

Finally, the multi-objective robust optimization model is established and solved by relevant optimization algorithms to obtain the ideal UTB, and realize the billet optimization of large-scale components.

Based on the above analyses, the UTB optimization procedure can be defined as an optimization criterion, which would provide an important guideline in the processing design of LTRC forming (Figure 24).

5 Conclusions

In this study, a multi-objective robust optimization approach for the size parameters of the UTB, accounting for the influence of uncertainties, was proposed to enhance the robustness of die rib-groove filling and strain homogeneity in the isothermal forging of Ti-alloy multi-rib eigenstructure. The main results are summarized as follows.

(1) Investigation of the material flow, rib-groove filling sequence, and strain inhomogeneity in the isothermal forging of the Ti-alloy multi-rib eigenstructure. The material exhibited transverse cross-rib flow at the web and longitudinal flow at the rib-groove in the die cavity, potentially resulting in a high level of effective strain with non-optimized billets.

(2) Utilization of image acquisition and perception to convert the forming state of the workpiece captured during the forming process into pixels through gray-scale transformation. This allowed for the calculation of the area and volume of the underfilling rate of the rib-groove based on pixel counts. With the support of IAPF, it was observed that certain rib-groove were filled before others by ETB, with an underfilling rate measured at 5.69% in that moment.

(3) Identification of significant factors affecting the rib-groove filling and strain inhomogeneity, which included die manufacturing deviation, billet manufacturing deviation, and friction factor. A robust optimization model based on the mean and variance of dual-RSM for the rib-groove filling and strain inhomogeneity of the Ti-alloy multi-rib

eigenstructure was developed. The correlation between the objective function and the size parameters of the billet under the fluctuation of uncertain factors was determined.

(4) Application of the NSGA-II algorithm and minimum distance method to optimize the UTB, achieving a reduction in underfilling rate by 4.66% and improvement in the strain homogeneity by 0.308 compared with the ETB outcomes.

(5) The comparison of optimized UTB between deterministic optimization and robust optimization indicated that the underfilling rate fluctuation reduced from 0.66 to 0.15 and strain homogeneity fluctuation reduced from 1.156 to 1.120. This indicated that the robust optimized UTB significantly improved the die rib-groove filling of the Ti-alloy multi-rib eigenstructure and led to the most homogeneous effective strain.

Acknowledgements
YH acknowledges the support of SNU Materials Education/Research Division for Creative Global Leaders of Republic of Korea.

Author Contributions
TD: Conceptualization, Methodology, Investigation, Simulation, Experiments, Writing, Review and Editing. KW: Methodology, Review and editing, Funding acquisition. YH: Methodology, Review and Editing. XD: Methodology, Review. LH: Methodology, Review. Myoung-Gyu Lee: Methodology, Review and Editing. All authors read and approved the final manuscript.

Funding
Supported by National Natural Science Foundation of China (Grant No. 52005241), Jiangxi Provincial Natural Science Foundation (Grant Nos. 20232BAB204050, 20224BAB204045), China Scholarship Council (Grant No. 202208360107).

Data Availability
Data will be made available on request.

Declarations

Competing interests
The authors declare no competing interets.

Received: 25 January 2024 Revised: 12 July 2024 Accepted: 22 July 2024
Published online: 27 August 2024

References

[1] W L Chan, M W Fu, J Lu, et al. Simulation-enabled study of folding defect formation and avoidance in axisymmetrical flanged components. *Journal of Materials Processing Technology*, 2009, 209: 5077-5086.
[2] K Wei, M Zhan, X G Fan, et al. Unequal-thickness billet optimization in transitional region during isothermal local loading forming of Ti-alloy rib-web component using response surface method. *Chinese Journal of Aeronautics*, 2018, 31: 845-859.
[3] S J Yuan, X B Fan. Developments and perspectives on the precision forming processes for ultra-large size integrated components. *International Journal of Extreme Manufacturing*, 2019, 1(2): 1-18.
[4] D Kampen, J Richter, T Blohm, et al. Design of a genetic algorithm to preform optimization for hot forging processes. *International Journal of Material Forming*, 2020, 13: 77-89.
[5] S Nayak, S A Kumar, H Gokhale, et al. Optimization of Ti-6Al-4V ring rolling process by FE simulation using RSM. *International Journal of Solids and Structures*, 2023, 262-263: 112064.
[6] Y Han, M Wang, Y F Chen, et al. Automatic preform design and optimization for aeroengine disk forgings. *The International Journal of Advanced Manufacturing Technology*, 2023, 125: 1845-1858.
[7] J Y Zheng, J Y C Fang, M W Fu. Flow-induced folding in multi-scaled bulk forming of axisymmetric flanged parts and its prediction and avoidance. *The International Journal of Advanced Manufacturing Technology*, 2022, 119: 5863-5883.
[8] K Wei, X G Fan, M Zhan, et al. Robust optimization of the billet for isothermal local loading transitional region of a Ti-alloy rib-web component based on dual-response surface method. *Frontiers of Mechanical Engineering*, 2018, 13: 376-384.
[9] J Cao, E Brinksmeier, M W Fu, et al. Manufacturing of advanced smart tooling for metal forming. *CIRP Journal of Manufacturing Science and Technology*, 2019, 68: 605-628.
[10] H G Zhang, M Zhan, Z B Zheng, et al. Development and challenge of forming manufacturing technologies for aerospace large-scale thin-wall axisymmetric curved-surface component. *Journal of Mechanical Engineering*, 2022, 58(20): 166-185.
[11] B Hou, W Wang, S Li, et al. Stochastic analysis and robust optimization for a deck lid inner panel stamping. *Material Design*, 2010, 31(3): 1191-1199.
[12] H Li, J Xu, H Yang, et al. Sequential multi-objective optimization of thin-walled aluminum alloy tube bending under various uncertainties. *Transactions of Nonferrous Metals Society of China*, 2017, 27(3): 608-615.
[13] C Y Park, J W Kim, B Kim, et al. Prediction for manufacturing factors in a steel plate rolling smart factory using data clustering-based machine learning. *IEEE Access*, 2020, 8, 60890-60905.
[14] T Q D Pham, T V Hoang, X V Tran, et al. A framework for the robust optimization under uncertainty in additive manufacturing. *Journal of Manufacturing Processes*, 2023, 103: 53-63.
[15] D N Bai, P F Gao, X G Yan, et al. Intelligent forming technology: State-of-the-art review and perspectives. *CIRP Journal of Manufacturing Science and Technology*, 2021, 1: 2021008-9.
[16] M Cuartas, E Ruiz, D Ferreño, et al. Machine learning algorithms for the prediction of non-metallic inclusions in steel wires for tire reinforcement. *Journal of Intelligent Manufacturing*, 2021, 32: 1739-1751.
[17] Z F Zhang, R Qin, G Li, et al. Deep learning-based monitoring of surface residual stress and efficient sensing of AE for laser shock peening. *Journal of Materials Processing Technology*, 2022, 303, 117515.
[18] H W Cho, S J Shin, G J Seo, et al. Real-time anomaly detection using convolutional neural network in wire arc additive manufacturing: Molybdenum material. *Journal of Materials Processing Technology*, 2022, 302: 117495.
[19] M Baral, J A Al, A Breunig, et al. Acoustic emission monitoring for necking in sheet metal forming. *Journal of Materials Processing Technology*, 2022, 310: 117758.
[20] P F Gao, X Yan, Y Wang, et al. An online intelligent method for roller path design in conventional spinning. *Journal of Intelligent Manufacturing*, 2022: 1-16.
[21] Z Gronostajski, Z Pater, L Madej, et al. Recent development trends in metal forming. *Archives of Civil and Mechanical Engineering*, 2019, 19(3): 898-941.
[22] H Li, J Yang, G Chen, et al. Towards intelligent design optimization: Progress and challenge of design optimization theories and technologies for plastic forming. *Chinese Journal of Aeronautics*, 2021, 34: 104-123.
[23] G Škulj, D Bračun. Geometry and temperature data fusion for automated measurement during open die forging of large hot workpieces. *Procedia CIRP*, 2020, 93: 1265-1268.
[24] L Liang, L Guo, Y Wang, et al. Towards an intelligent FE simulation for real-time temperature-controlled radial-axial ring rolling process. *Journal of Manufacturing Processes*, 2019, 48: 1–11.
[25] J Repalle, R V Grandhi. Design of forging process variables under uncertainties. *Journal of Materials Engineering and Performance*, 2005, 14(1): 123-131.

[26] T Ding, K Wei, C Yang, et al. Robust optimization of consistency in filling of rib-grooves for titanium alloy multi-rib eigenstructure. *The International Journal of Advanced Manufacturing Technology*, 2023: 1-20.
[27] N Ben, Q Zhang, K Bandyopadhyay, et al. Analysis of friction behaviour under oscillating forming process using T-shape compression test and finite element simulation. *Journal of Materials Processing Technology*, 2020, 275: 116327.
[28] A Ducato, G Buffa, L Fratini, et al. Dual phase titanium alloy hot forging process design: experiments and numerical modeling. *Advances in Manufacturing*, 2015, 3: 269-281.
[29] H Sofuoglu, J Rasty. Flow behavior of Plasticine used in physical modeling of metal forming processes. *Tribology International*, 2000, 33(8): 523-529.
[30] Z Sun, J Cao, H Wu, et al. Inhomogeneous deformation law in forming of multi-cavity parts under complex loading path. *Journal of Materials Processing Technology*, 2018, 254: 179-192.
[31] J Cao, Z Sun, Z K Yin, et al. Forming feasibility of complex multi-cavity parts of 316LN steel by multi-direction loading: from aspect of geometric and process parameters. *Journal of Materials Processing Technology*, 2020, 109: 261-273.
[32] H Sofuoglu, H Gedikli. Physical and numerical analysis of three dimensional extrusion process. *Computational Materials Science*, 2004, 31: 113-124.
[33] K Eckerson, B Liechty, C D Sorensen, et al. Thermomechanical similarity between Van Aken plasticine and metals in hot-forming processes. *The Journal of Strain Analysis for Engineering Design*, 2008, 43: 383-394.
[34] T Robinson, H Ou, C G Armstrong. Study on ring compression test using physical modelling and FE simulation. *Journal of Materials Processing Technology*, 2004, 153-154: 54-59.
[35] C K Shih, C H Hung. Experimental and numerical analyses on three-roll planetary rolling process. *Journal of Materials Processing Technology*, 2003, 142: 702-709.
[36] C H Jeon, S W Han, B D Joo, et al. Deformation analysis for cold rolling of Al-Cu double layered sheet by physical modeling and finite element. *Metals and Materials International*. 2013, 19(5): 1069-1076.
[37] F F Saniee, I Pillinger, P Hartley. Friction modelling for the physical simulation of the bulk metal forming process. *Journal of Materials Processing Technology*, 2004, 153: 151-15.
[38] M Li, Z Liu, L Huang, et al. Multi-fidelity data-driven optimization design framework for self-piercing riveting process parameters. *Journal of Manufacturing Processes*, 2023, 99: 812-824.
[39] K Wei, X G Fan, M Zhan, et al. Uncertainty analysis and multi-objective billet robust optimization for transitional region of multi-rib component under isothermal local loading forming. *The International Journal of Advanced Manufacturing Technology*, 2018, 97: 1165-1179.
[40] C Chen, S Zhao, X Han, et al. Optimization of a reshaping rivet to reduce the protrusion height and increase the strength of clinched joints. *Journal of Materials Processing Technology*, 2016, 234: 1-9.
[41] P F Gao, X Li, H Yang, et al. Influence of die parameters on the deformation inhomogeneity of transitional region during local loading forming of Ti-alloy rib-web component. *The International Journal of Advanced Manufacturing Technology*, 2017, 90: 2109-2119.
[42] Y H Yang., D Liu, Z Y He, et al. Optimization of preform shapes by RSM and FEM to improve deformation homogeneity in aerospace forgings. *Chinese Journal of Aeronautics*, 2010, 23: 260-267.
[43] X Li, C Sun, L Qian, et al. Flow defects of rib-web components in isothermal local-loading forming process. *The International Journal of Advanced Manufacturing Technology*, 2023, 125: 3417-3429.
[44] S L C Ferreira, R E Bruns, H S Ferreira, et al. Box-Behnken design: An alternative for the optimization of analytical methods. *Analytica Chimica Acta*, 2007, 597: 179-186.
[45] L H Wang, H C Amos, K Deb. Multi-objective evolutionary optimisation for product design and manufacturing. *Assembly Autom*, 2011, 32(4): 597~603
[46] G Zhao, H Chen, C Zhang, et al. Multi-objective optimization design of porthole extrusion die using Pareto-based genetic algorithm. *The International Journal of Advanced Manufacturing Technology*, 2013, 69: 1547-1556.
[47] Y Yao, D L Ma, M Q Yang, et al. Adaptive-surrogate-based robust optimization of transonic natural laminar flow nacelle. *Chinese Journal of Aeronautics,* 2021, 34: 36-52.
[48] H Zhang, Y Liu, C Liu. Multi-objective parameter optimization for cross-Sectional deformation of double-Ridged rectangular tube in rotary draw bending by using response surface methodology and NSGA-II. *Metals*, 2017, 7(6): 206.
[49] D W Zhang, H Yang, Z C Sun. Analysis of local loading forming for titanium-alloy T-shaped components using slab method. *Journal of Materials Processing Technology.* 2010, 210: 258-266.

Tong Ding born in 1997, is currently a PhD at *School of Materials Science and Technology, Nanjing University of Aeronautics and Astronautics, China*. He received his MS degree from *Nanchang Hangkong University, China*, in 2024. His research interests include precision forming technology of aerospace components.

Ke Wei born in 1986, is an associate professor at *Nanchang Hangkong University, China*. His main research interest is numerical simulation of plastic forming.

Yong Hou born in 1993, is currently an Alexander von Humboldt (AvH) fellow at Technische Universität Dortmund, Germany. Dr. Hou got his PhD degree at Tongji University, China, in 2021. His main research interests are metal forming and constitutive modeling.

Xianjuan Dong born in 1979, is an associate professor at *Nanchang Hangkong University, China*. Her main research interest is metal plasticity theory and technology.

Long Huang born in 1986. He received his PhD from *Northwestern Polytechnical University, China,* in 2022. His main research interest is digital technology of material processing.

Myoung-Gyu Lee born in 1974. is currently a full professor in the *Department of Materials Science and Engineering, Seoul National University, Republic of Korea*. His main interest in research includes the multiscale–multiphysics modeling and simulations of structural materials for optimizing manufacturing processes, plasticity theory, and constitutive model development for highly nonlinear and anisotropic metals.